

UNIVERSITY OF CALGARY

Application of a finite-difference scheme

for the time-domain computation of 1D anelastic wavefields to fractured media.

by

Pedro Enrique Martinez Fernandez

A THESIS

SUBMITTED TO THE FACULTY OF GRADUATE STUDIES
IN PARTIAL FULFILLMENT OF THE REQUIREMENTS FOR THE
DEGREE OF MASTER OF SCIENCE

DEPARTMENT OF GEOSCIENCE

CALGARY, ALBERTA

June, 2014

© Pedro Enrique Martinez Fernandez 2014

Abstract

In this work, I develop a 1D finite-difference formulation that is capable of simulating non-welded contact boundary conditions in anelastic media. I include, in the linear-slip boundary conditions for non-welded contact, the memory variables that are obtained as a result of considering a generalized Maxwell rheology. Then I proceed to obtain a heterogeneous formulation which is a result of the introduction of a fictitious points scheme for the boundary conditions. In other words I obtain a generalized homogeneous formulation. I solve the resulting system of equations and substitute the amplitudes obtained into the equation of motion.

I analyze the numerical results obtained and compare these with an analytical solution and two other anelastic formulations for the welded contact case. I examine different scenarios such as anelastic-anelastic and elastic-anelastic wave propagation in welded and non-welded contact by looking at the transmitted and reflected pulse in welded as well as non-welded contact.

Acknowledgements

The result of this research would not have been possible without the support of many people. First and foremost I would like to express my gratitude to my supervisor Dr. Edward Krebes for his support, guidance and patience through this journey. I would like to thank him for proofreading and corrections made to this work. His invaluable advice and example have always motivated me to achieve higher goals and excel in my academic and professional life.

In the Department of Geoscience to all the professors, staff and students with whom I have shared these two wonderful years. Thanks to Larry Lines, Robert Ferguson, Adam Pidlisecky, John Bancroft and Kris Inananen. I have learned a lot from all of them. Special thanks to Cathy Hubbell for all the instances in which their assistance helped me along the way.

I would also like to thank to my mentor Anibal Trista for his decisive encouragement and motivation to pursuit a career in Geophysics. For taking me like a member of his family. I owe him a lot.

My deepest gratitude to Jorge Carrillo for putting his faith in me. His example and encouragement has been decisive in my life.

A very special thanks to Gabino Castillo who during his short visits to Calgary always has some time to share with me. Thank you very much my friend.

Special thanks to Juan José Gómez for his teachings about hard work and his support during my stay in Villahermosa.

To Nilda Alfonso who has been my guardian angel, thank you very much for everything.

The present work is dedicated to Frank Bejerano and Vilma Fernández because without them this dream could have never been possible.

Table of Contents

Abstract	ii
Acknowledgements	iii
Table of Contents	iv
List of Figures	v
List of Symbols	vii
1 INTRODUCTION	1
1.1 DESCRIPTION OF THE PROBLEM	1
1.2 OUTLINE OF THE THESIS	3
2 NON-WELDED CONTACT	5
2.1 INTRODUCTION	5
2.2 THE LINEAR SLIP MODEL	5
2.3 MODELING THE NON-WELDED CONTACT	9
3 ANELASTIC ISOTROPIC WAVE MODELING	13
3.1 INTRODUCTION	13
3.2 LINEAR VISCOELASTIC MODELS	14
3.3 STRAIN-STRESS RELATION FOR ANELASTIC MEDIA	16
3.4 THE EK METHOD	18
3.5 FINITE DIFFERENCE IMPLEMENTATION OF ANELASTIC WAVE MODELING	25
4 MODELING FRACTURES IN ANELASTIC ISOTROPIC MEDIA	31
4.1 INTRODUCTION	31
4.2 THE FICTITIOUS POINTS SCHEME APPLIED TO THE MODELING OF NON-WELDED CONTACT IN ANELASTIC MEDIA	32
5 NUMERICAL SIMULATION OF NONWELDED CONTACT IN ANELASTIC ISOTROPIC MEDIA	37
5.1 INTRODUCTION	37
5.2 DESCRIPTION OF THE NUMERICAL MODEL	37
5.3 EFFECT OF COMPLIANCE ON THE REFLECTED WAVE	46
5.4 EFFECT OF THE COMPLIANCE ON THE TRANSMITTED WAVE	52
5.5 EFFECT OF THE ANELASTICITY IN THE TRANSMITTED WAVE	56
5.6 EFFECT OF THE ANELASTICITY IN THE REFLECTED WAVE	58
5.7 NON-WELDED CONTACT LAYERED MEDIUM	60
6 CONCLUSIONS	64

List of Figures and Illustrations

2.1	Schematic of a fracture with monoclinic behavior (Schoenberg and Douma, 1988)	7
2.2	Schematic of a fracture with orthorhombic behavior (Schoenberg and Douma, 1988)	8
2.3	Schematic of the fictitious points scheme for the calculation of the non-welded contact. ρ and β represent the densities and velocities of both media. The circles represent the location of the real displacements (u_n) while crosses represents the locations of fictitious displacements (\tilde{u}_n) on both sides of the boundary.	12
3.1	The Voigt model unit, where η is the viscosity in the dashpot and M is the spring constant or elastic modulus.	14
3.2	The Maxwell model unit, where η is the viscosity in the dashpot.	15
3.3	The Maxwell model unit response (Nowick and Berry, 1972)	15
3.4	The <i>Standard Linear Solid</i> or <i>SLS</i>	16
3.5	The generalized Maxwell body or Maxwell-Wiechert model. In the figure the elastic moduli and viscosities are represented by springs and dashpots respectively.	20
3.6	The relaxation function represented as an exponential decay function. The subscripts "U" and "R" indicate unrelaxed and relaxed respectively	22
3.7	The generalized Maxwell body or Maxwell-Wiechert model. In the figure the elastic moduli and viscosities are represented by springs and dashpots respectively.	24
3.8	Problem geometry and model.	29
3.9	Top: Pulse used in the simulations. Bottom: Amplitude spectrum of the pulse.	29
3.10	Comparison of the Emmerich and Korn method and the standard method proposed by Krebes and Quiroga-Goode	30
3.11	Comparison of the Emmerich and Korn method and the standard method proposed by Krebes and Quiroga-Goode. Detail of the reflection produced at the first interface.	30
4.1	Schematic of the fictitious points scheme for the calculation of the non-welded contact. The circles represent the location of the displacements on both sides of the fracture while the arrows represents the stresses on both sides of the boundary.	33
4.2	Stencil used in the formulation of the generalized homogeneous finite difference scheme.	36
5.1	Problem geometry and model used in the numerical simulations.	39
5.2	Top: Pulse used in the simulations. Bottom: Amplitude spectrum of the pulse.	40
5.3	Comparison of the three methods with $\eta_N = 0$ (welded contact case). All graphs are normalized to a maximum amplitude of unity.	41

5.4	Comparison of the three methods with $\eta_N = 0$ (welded contact case). Detail of the first reflection. All graphs are normalized to a maximum amplitude of unity.	42
5.5	Comparison of the three methods with $\eta_N = 0$ (welded contact case). Detail of the second reflection. All graphs are normalized to a maximum amplitude of unity.	43
5.6	Graph of the difference between the generalized finite difference method and the EK and standard method for welded contact.	44
5.7	Graph of the absolute value of the difference between the generalized finite difference method and the EK and standard method.	45
5.8	Comparison between the FD for the welded contact case (solid line) and the analytical solution (dashed line). Both graphs are normalized to a maximum amplitude of unity.	46
5.9	Effect of compliance on the reflected wave coming from the first interface. . .	48
5.10	Reflection from the first interface for a range from 0.001 to 0.005.	49
5.11	Effect of compliance on the reflected wave coming from the second interface. As the first fracture becomes decoupled less energy is transmitted to the second interface.	50
5.12	Effect of compliance on the reflected wave coming from the first interface (solid line) compared to the analytical solution (dashed line)	51
5.13	Problem geometry and model for the transmitted wave.	53
5.14	Effect of compliance on the transmitted wave.	54
5.15	Effect of compliance on the power spectrum of the transmitted wave. The increase of the compliance values act as a low-pass filter for the pulse.	55
5.16	Effect of viscoelasticity on the transmitted wave compared to the effect of the non-welded contact between two elastic media. For the anelastic case the value of Q is the same for both layers.	57
5.17	Effect of viscoelasticity on the reflected wave compared to the effect of the non-welded contact between two elastic media.	58
5.18	The graph shows the reflected wave produced by an interface located between an elastic incident medium and an anelastic transmitted medium. In the upper section the interface between the two media is in non-welded contact for values of the compliance around $0.015m/GPa$. The lower section shows the seismic response when the interface between the two media is in welded contact.	59
5.19	The upper section shows an elastic model where every boundary is in non-welded contact and the background medium is elastic. The lower section shows an anelastic medium with every interface in welded contact.	60
5.20	The upper section show the different waveforms of the direct wave for different values of the compliance assuming every boundary of the grid in non-welded contact in the elastic medium. The lower section show the different waveforms of the direct wave for different values of Q in an anelastic medium.	62
5.21	Travel-time delay vs compliance showing a linear dependence between the two factors.	63

List of Symbols, Abbreviations and Nomenclature

Symbol	Definition
U of C	University of Calgary
τ	complex phase function
ω	radial frequency
f	linear frequency
$\iota = \sqrt{-1}$	
ϵ	strain
σ	stress
Q	quality factor
$R(t)$	relaxation function
v	wave speed
M_R	relaxed modulus
M_U	unrelaxed modulus
$M(\omega)$	viscoelastic modulus
$r(\omega)$	normalized relaxation spectrum
ζ	memory variable
Im	imaginary part
Re	real part
J	number of relaxation mechanisms
μ	rigidity in the medium
ρ	density
ξ	memory variable
\hat{p}	Courant number
β	elastic (unrelaxed) wave velocity

η	compliance
κ	stiffness
γ	viscosity
<i>NWC</i>	Non-welded contact
<i>WC</i>	Welded contact
<i>WC</i>	Welded contact
<i>EK</i>	Emmerich and Korn method
<i>STD</i>	Strandard method (by Krebs and Quiroga-Goode)

Chapter 1

INTRODUCTION

1.1 DESCRIPTION OF THE PROBLEM

An interesting kind of problem in seismology arises from the presence of non-welded contact at geological interfaces in seismic forward modeling problems. The theory of non-welded contact is an ideal representation of a fracture in a medium. In other words the displacement discontinuity at the interface, due to non-welded contact, is a function of traction at a specific point along the contact. In addition stress and strain are bound by a linear relation. However this is not merely a theoretical problem. Hydrocarbon production from unconventional sources, such as shale gas and oil, is heavily dependent on the characteristics of the reservoir. It is crucial to know to what extent the reservoir is naturally fractured in order to maximize production and therefore efficiency. In addition, injection and production practices also create man-made fractures that can alter the seismic response of the reservoir in an ulterior stage of seismic monitoring. The presence of complex fracture systems in different types of reservoirs can have a significant impact in the fluid flow and therefore presents a great technical challenge. In consequence the study of attenuation due to the presence of fractures and the characterization of their seismic response are of special importance. In addition, absorption occurs due to other physical phenomena that contribute to loss of energy as a wave propagates through real media such as heavy oil reservoirs (Behura et al., 2007). Besides geometrical spreading and energy partitioning, frictional effects caused by anelastic properties of the medium also play a very important role in absorption. Therefore it is very important to obtain a single formulation to characterize the combined seismic response of these two effects simultaneously rather than separately.

Understanding wave propagation phenomena is of utmost importance for complementing

our knowledge of geological systems. In this regards modeling of geophysical problems by means of numerical methods can not only offer a detailed perspective of the problem at hand but in addition does it at a fraction of the cost involved in the exploration of a certain geological feature. Multiple approaches to the solution of this problem have been proposed in the existing literature. Some of the most important ones are ray theory, the finite element, matrix propagation and finite difference methods. These methods have the advantage of modeling numerical experiments under well defined and conveniently chosen parameters such as source excitation mechanism, grid size and boundary conditions. With the inclusion of complex rheologies accounting for factors such anisotropy, elasticity, anelasticity, scattering from heterogeneities and poroelasticity, seismic wave modeling has been growing in terms of complexity. However new computer technology and the ever growing capabilities in data processing and storage have also made possible the study of wave propagation phenomena from new perspectives given the increase in dimensionality and frequency resolution.

In order to study absorption in media due to viscoelasticity, numerical modeling of seismic wave propagation is also one the most important tools to use and validate the predicted models and rheologies. Anelasticity in media causes seismic waves traveling through them to lose energy, and it induces velocity dispersion (the variation of velocity with frequency). There are different methods for including anelastic effects in numerical simulations. The theory of viscoelasticity is typically used to model anelastic effects in media. These methods can be divided mainly into two groups: pseudo-spectral and time-domain methods. In the first group spatial derivatives are calculated by Fourier transforms and marched in time. In the latter group one transforms the convolution integral describing viscoelastic effects into something that can be implemented in a numerical scheme, such as a method that transforms it into a convergent sequence by Padé approximants (Day and Minster, 1984), and a method that employs a combination of finite integral transforms and finite difference methods in order to obtain the total seismic wave field by means of solving hyperbolic partial

differential equations (Mikhailenko, 1985). Another method incorporates a rheological model of a viscoelastic medium which consists of a network of springs and dashpots, such as the model known as the generalized Maxwell body (Emmerich and Korn, 1987). Other studies on this topic have also been conducted by Tal-Ezer et al. (1990) and Carcione et al. (1988). The later uses pseudo-spectral time and space integration techniques to solve the first-order differential equation of motion and avoid numerical dispersion (Carcione et al., 1988).

In this work an generalized homogeneous finite difference formulation for the anelastic case is obtained. It is shown that this formulation yields similar results to the ones developed by (Emmerich and Korn, 1987) and (Krebes and Quiroga-Goode, 1994) for the case of welded contact.

1.2 OUTLINE OF THE THESIS

Chapter 2 introduces the linear slip formulation for non-welded contact. Several possible formulations of the interface compliance tensor are explored for the different fracture systems. Following the approach of Korn and Stöckl (1982) finite difference expressions for the boundary conditions at the interfaces are obtained for the elastic case as a first step into my extension of this method to anelastic media.

In Chapter 3 several models that describe the problem of linear viscoelasticity are revisited. In this chapter, the linear theory of viscoelasticity for the generalized Maxwell body (after Emmerich and Korn, 1987) is introduced and a finite difference scheme based on the consecutive application of the central difference operator to spatial derivatives by Krebes and Quiroga-Goode (1994) is explained and compared with the Emmerich and Korn approach.

Chapter 4 describes in detail the finite difference formulation of the second order hyperbolic differential equation that governs seismic wave propagation in a 1-D heterogeneous anelastic medium that incorporates non-welded contact. The starting point for the development of this formulation can be found in the works of Korn and Stöckl (1982), Emmerich

and Korn (1987) and Krebs and Quiroga-Goode (1994). Implicit boundary conditions are imposed to simulate the linear slip formulation and therefore non-welded contact. As a result a generalized finite difference scheme is obtained and the results agree very closely with the previous formulations for the welded contact case.

In Chapter 5 numerical results for different values of the stiffness or compliance of a 1D simple model are displayed and analyzed. In addition some comparison is attempted with results based on experimental results carried in laboratory conditions by Pyrak-Nolte et al. (1990). The algorithm is also compared with a ray-tracing method that incorporates both anelasticity and non-welded contact.

Chapter 6 presents the conclusions of this work.

Chapter 2

NON-WELDED CONTACT

2.1 INTRODUCTION

In general, for a flat interface between two geological layers, if all of the area of the two different surfaces is in contact we are in the presence of a welded contact boundary. If there are voids in the area of the contact plane then it is said that we are in the presence of a non-welded contact. An example of this would be a fracture. An important problem in reservoir characterization is the determination of the orientations of sets of fractures. A medium with fractures can be modeled as an elastic or viscoelastic anisotropic medium. The analysis of anisotropy in seismic data can yield information on the presence and orientations of sets of fractures.

A set of fractures in a medium introduces anisotropy in the effective elastic moduli and therefore velocities will vary according to the direction of propagation. Fractures at different scale levels, from microfractures to crustal faults, affect wave propagation by slowing down and attenuating waveforms. In particular, it has been observed that single fractures can reflect up to 96% of the energy of incident waves (Pyrak-Nolte et al., 1990). In order to correctly interpret seismic data such effects must be taken into account.

2.2 THE LINEAR SLIP MODEL

An excellent approximation to the modeling of real fractures has been obtained by Schoenberg (1980), who proposed a model for an imperfectly bonded interface between two media. This model consisted of the assumption that the displacement discontinuity is linearly related to the traction across the boundary at every point and can be represented with an

expansion series of the form

$$T_i = T_i^0 + \kappa_{ij}\Delta u_j + O(\Delta u)^2, \quad (2.1)$$

where κ_{ij} are the elements of the boundary stiffness matrix with dimensions of stress/length, T_i are the components of the traction vector, u_j are the components of the particle displacement and where a doubly repeated subscript in a term, e.g., j , indicates a sum from 1 to 3 over that term. $T_i^0 = 0$ due to the requirement that $\Delta u_i = 0$ if $T_i = 0$. The stiffness of the fracture depends on the spatial distribution of the void spaces and the amount of contact between media within the fracture (Pyrak-Nolte, 1996). To be consistent with a linear approximation to the problem, quadratic and higher order terms are neglected. A more general equation was obtained by Pyrak-Nolte (1988) and Carcione (1996) that considers the presence of a liquid under saturated conditions in the fracture. This increases the specific stiffness and viscous coupling between the two surfaces in contact (Pyrak-Nolte et al., 1990).

$$T_i = \kappa_{ij}\Delta u_j + \gamma_{ij}\Delta v_j, \quad (2.2)$$

where Δv_j , and γ_{ij} are the particle velocity discontinuity and the elements of the specific viscosity tensor. This equation describes a more realistic fracture when a liquid at the interface produce a viscoelastic coupling. If $\gamma_{ij} = 0$ then the equation describes only the displacement discontinuity case or dry fracture.

The displacement discontinuity problem can also be conveniently represented by using the interface compliance tensor where their elements are related to the elements of the stiffness matrix by the expression $\eta_{ij} \equiv \kappa_{ij}^{-1}$

$$\Delta u_i = \eta_{ij}T_j. \quad (2.3)$$

The form of the interface compliance tensor changes depending on the fracture system to be represented. In a homogeneous medium six parameters are required to describe the

fracture behavior. This is the case of the triclinic fracture system of anisotropy. In order to simplify the problem, fracture systems are usually described by three symmetry classes, therefore reducing effectively the number of independent parameters in systems of equations that arise in the theory. These are the monoclinic, orthorhombic and the transversely isotropic fracture classes.

In the monoclinic fracture system the fracture system is invariant to a reflection about a plane containing the x_3 component. If for example, this plane is the $x_1 - x_3$ plane then η_{ij} has the following form

$$\boldsymbol{\eta} = \begin{bmatrix} \eta_1 & 0 & \eta_{1n} \\ 0 & \eta_2 & 0 \\ \eta_{1n} & 0 & \eta_n \end{bmatrix}, \quad (2.4)$$

where η_n and η_2 are the normal compliance and the compliance in the x_2 direction. The term η_{n1} represents the coupling of the x_1 -tangential slip and the normal compliance. This means that a opening or closure of the fracture will cause tangential slip in the x_1 direction (Schoenberg and Douma, 1988).

This form of the tensor shows that slip in the x_2 -direction is uncoupled from both normal and tangential slip in the x_1 -direction. Normal and tangential components of slip are coupled due to the corrugation of the contact surfaces rather than the material filling the fracture. Figure 2.1 shows a schematic of this type of system.

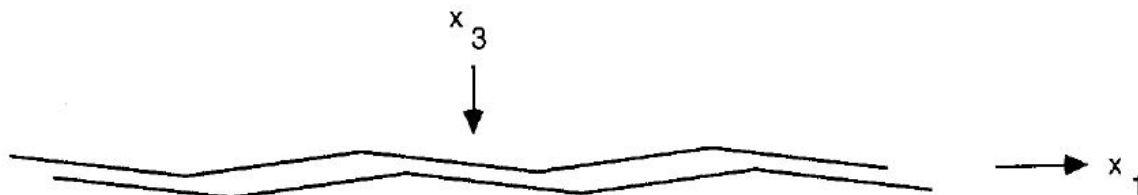


Figure 2.1: Schematic of a fracture with monoclinic behavior (Schoenberg and Douma, 1988)

The orthorhombic fracture system represents the case when the system is invariant to a reflection about a plane not containing the x_3 component, namely the $x_1 - x_2$ plane. In this case the normal and tangential displacements to the fractures are uncoupled, and η has the form

$$\boldsymbol{\eta} = \begin{bmatrix} \eta_1 & \eta_{12} & 0 \\ \eta_{12} & \eta_2 & 0 \\ 0 & 0 & \eta_n \end{bmatrix}, \quad (2.5)$$

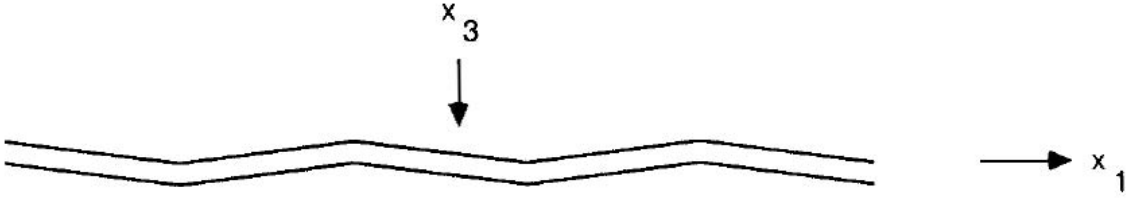


Figure 2.2: Schematic of a fracture with orthorhombic behavior (Schoenberg and Douma, 1988)

Finally when the fracture system is invariant to a rotation around the x_3 axis we are in presence of the transversely isotropic fracture system. This is the most symmetric case which offers a unique opportunity for its implementation in a finite difference code due to its simplicity. For this case η has the form

$$\boldsymbol{\eta} = \begin{bmatrix} \eta_t & 0 & 0 \\ 0 & \eta_t & 0 \\ 0 & 0 & \eta_n \end{bmatrix}, \quad (2.6)$$

where η_n and η_t are the normal and tangential compliances. The tangential fracture displacement and the tangential component of the stress traction are linearly related and the normal and tangential compliances are uncoupled. If both compliances in this case are

equal to 0 then we are in presence of the welded contact case where the interface is perfectly bonded.

Experimental results have confirmed that the effects of a fracture can be analyzed by means of a non-welded contact where seismic stress is continuous across the boundary and the particle displacement presents a discontinuity equal to the ratio of the stiffness of the material and the stress (Pyrak-Nolte et al., 1990). The theoretical and measured values of spectral amplitudes in these experiments showed a correlation coefficient of 0.98 thus suggesting that the linear slip model is able to accurately model a real fracture.

2.3 MODELING THE NON-WELDED CONTACT

There are several methods in the literature that describe the numerical modeling of the non-welded contact. A number of them make use of finite difference techniques. Coates and Schoenberg implement the linear deformation model using a staggered-grid. However in this approach different elements of the elastic modulus matrix are required at different locations in the grid requiring more detailed information on the location of the interface (Coates and Schoenberg, 1995). In particular the off-diagonal stress and strain components are not defined at the same location. This requires interpolation of the aforementioned components in order to solve the stress-strain relation (Carcione et al., 2002). Another approach is the boundary element method. In this method the only discretization is done at the fracture (Gu et al., 1997). Carcione (1996) introduced a convolutional model to account for displacement and velocity discontinuity effectively including anelasticity at the interface only. However the numerical algorithm was based in a domain decomposition method rather than a finite difference one (Carcione, 1996), (Carcione et al., 2012). Using this methodology Carcione et al. (2012) proved that a set of equispaced plane fractures in an homogeneous lossless background medium is transversely isotropic and viscoelastic.

Here the approach of Korn and Stöckl 1982 is followed in order to obtain finite difference

expressions for the boundary conditions at the interface using finite differences and the fictitious point scheme. In the following example the case of a fracture being modeled between two elastic media is considered.

For simplicity let's consider a SH wave propagating in the xz -plane with the displacement given by the y -component. In addition consider a non-welded interface located at $z_{n+1/2} = (n + 1/2)\Delta z$, where n is an integer representing a grid point and Δz is the grid step size in the z direction. Then,

$$u_y^+ - u_y^- = \eta_t \sigma_{yz}, \quad (2.7)$$

where u_y^+ and u_y^- represent the displacement evaluated on both sides of the boundary. The $+$ superscript refers to quantities evaluated at $z > z_{n+1/2}$ while the $-$ superscript refers to quantities located at $z < z_{n+1/2}$. In this equation η_t is the tangential compliance factor. In order to model the non-welded contact a row of fictitious points is introduced in such a form that medium 1 is extended into medium 2 and vice-versa (Korn and Stöckl, 1982), as can be seen in Figure 2.3. If we consider the boundary at $n + 1/2$ then we can write the boundary condition for the non-welded contact case, with displacements to $O(\Delta z)^2$, as (Slawinski, 1999)

$$\frac{1}{2}(u_{n+1} + \tilde{u}_n) - \frac{1}{2}(\tilde{u}_{n+1} + u_n) = \eta_t \mu^+ \left(\frac{u_{n+1} - \tilde{u}_n}{\Delta z} \right), \quad (2.8)$$

where \tilde{u}_n and \tilde{u}_{n+1} are the displacements at the fictitious points or locations and μ is the *Lamé* constant, i.e., the shear modulus. In this work the z axis will be always be pointing downwards. For the stress boundary condition the following equation can be written

$$\mu^+ \left(\frac{u_{n+1} - \tilde{u}_n}{\Delta z} \right) = \mu^- \left(\frac{\tilde{u}_{n+1} - u_n}{\Delta z} \right). \quad (2.9)$$

This system of equations can be solved to yield explicit solutions for \tilde{u}_n and \tilde{u}_{n+1} in terms of the displacements at the real points

$$\tilde{u}_n = \frac{2\mu^-u_n + (\mu^+ - \mu^- + 2\eta_t\mu^+\mu^-/\Delta z)u_{n+1}}{\mu^+ + \mu^- + 2\eta_t\mu^+\mu^-/\Delta z}, \quad (2.10)$$

$$\tilde{u}_{n+1} = \frac{2\mu^+u_{n+1} - (\mu^+ - \mu^- - 2\eta_t\mu^+\mu^-/\Delta z)u_n}{\mu^+ + \mu^- + 2\eta_t\mu^+\mu^-/\Delta z}. \quad (2.11)$$

If the compliance $\eta_t = 0$ then the aforementioned equations reduce to the case of the welded contact

$$\tilde{u}_n = \frac{2\mu^-u_n + (\mu^+ - \mu^-)u_{n+1}}{\mu^+ + \mu^-}, \quad (2.12)$$

$$\tilde{u}_{n+1} = \frac{2\mu^+u_{n+1} - (\mu^+ - \mu^-)u_n}{\mu^+ + \mu^-}. \quad (2.13)$$

If $\mu^+ = \mu^- = \mu$ but $\eta_t \neq 0$, then the media present no material discontinuity across the boundary, therefore the difference between displacement at real and fictitious points is parameterized by the parameter $\eta_t\mu/\Delta z$. The equations can be written then in the form

$$\tilde{u}_n = \frac{u_n + (\eta_t\mu/\Delta z)u_{n+1}}{1 + \eta_t\mu/\Delta z}, \quad (2.14)$$

$$\tilde{u}_{n+1} = \frac{u_{n+1} - (\eta_t\mu/\Delta z)u_n}{1 + \eta_t\mu/\Delta z}. \quad (2.15)$$

If $\mu^+ = \mu^- = \mu$ and the compliance $\eta_t = 0$ simultaneously then

$$\tilde{u}_n = u_n, \quad (2.16)$$

$$\tilde{u}_{n+1} = u_{n+1}. \quad (2.17)$$

The aforementioned result implies that for a homogeneous medium, with no discontinuity in the displacement caused by the presence of a fracture, the value of the displacements at the fictitious points is reduced to the values of the real points in the medium.

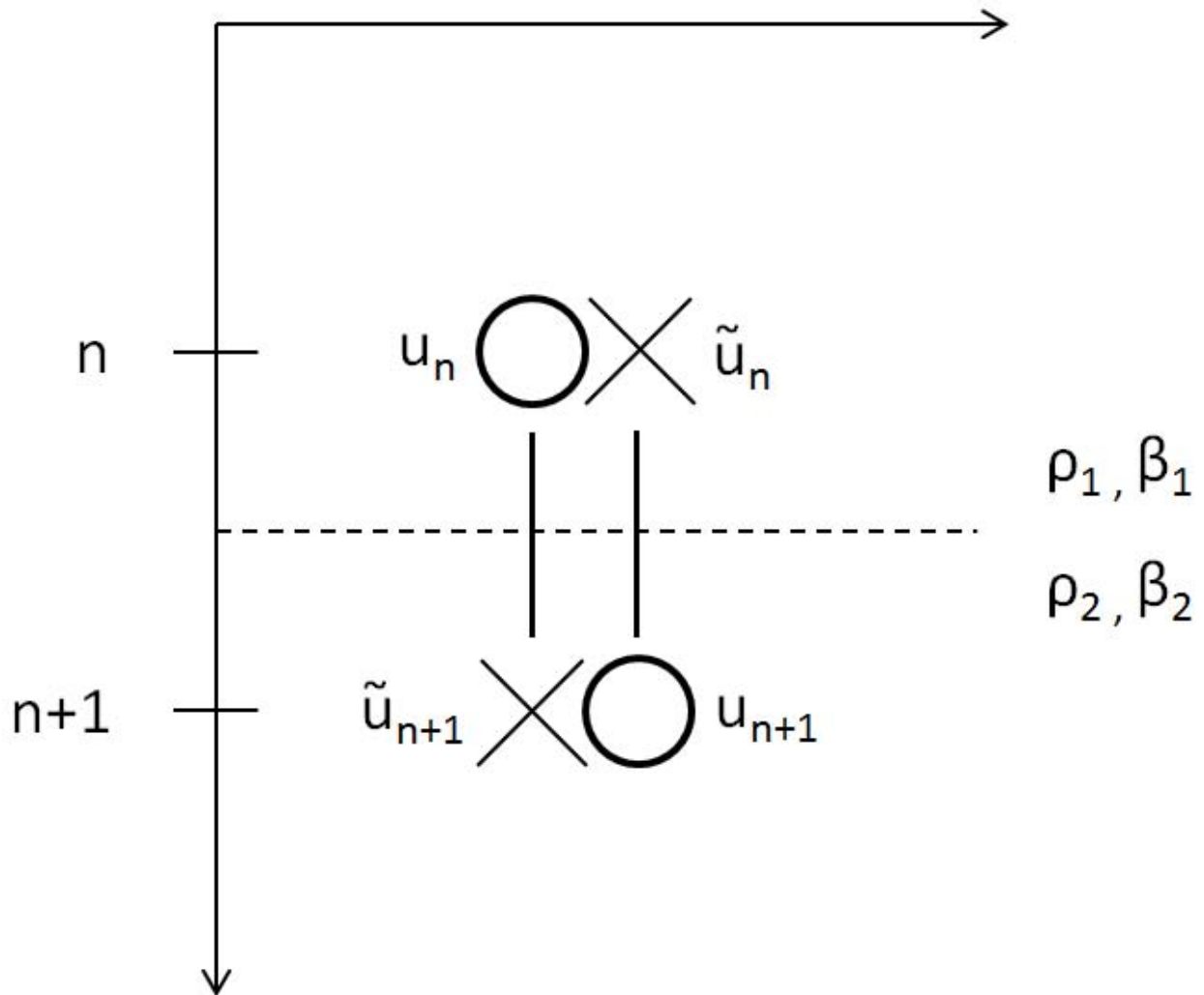


Figure 2.3: Schematic of the fictitious points scheme for the calculation of the non-welded contact. ρ and β represent the densities and velocities of both media. The circles represent the location of the real displacements (u_n) while crosses represents the locations of fictitious displacements (\tilde{u}_n) on both sides of the boundary.

Chapter 3

ANELASTIC ISOTROPIC WAVE MODELING

3.1 INTRODUCTION

Real media exhibit a wide set of physical phenomena related to the intrinsic properties of the media. Effects such as amplitude attenuation due to wave energy absorption, waveform phase changes and broadening of the waveform are among the well-known effects that can be identified in seismic data due to internal friction or anelasticity. The term anelasticity is used to describe a medium where the deformation is dependent not only on the stress, but also on the rate of change of the stress with time. This capacity of real media to dissipate vibrational energy is important for calculating several key material properties of a medium. Measurement of the attenuation of wave energy as it travels through a medium can yield information about the physical properties of the material through which the wave has traveled.

Several phenomenological models of a medium have been proposed to take these effects into account. The proposed models consist in a series of combinations of springs and dashpots that includes a time delay in the return to the equilibrium of the system. It is important to take into consideration that anelasticity does not mean "non-elastic" for the entire response of the media but only for a small fraction of the total response (Nowick and Berry, 1972).

The proposed models that represent the behavior of anelastic media will be revisited in this chapter. This will allow us to find a suitable expression for the stress that can be used along with the stress-strain relation to obtain a finite difference formulation for the modeling of wave propagation in linear viscoelastic media.

3.2 LINEAR VISCOELASTIC MODELS

The phenomenological description of anelastic media can be achieved by combining into a single model viscous and elastic elements. These models are built based on a combination of springs and dashpots in series or parallel. There are two basic linear viscoelastic models whose difference lies in the disposition of the elements. The Voigt model features a dashpot and a spring element in parallel as can be seen in figure 3.1.

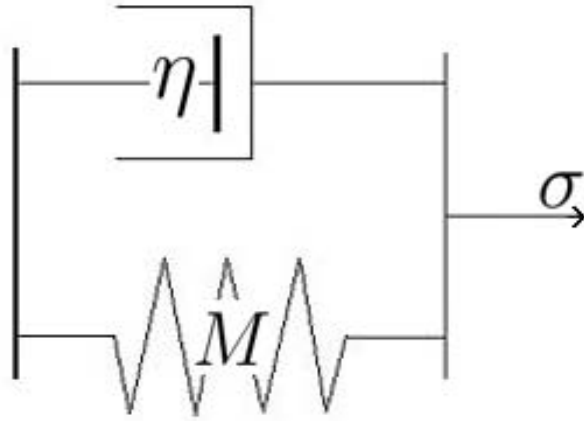


Figure 3.1: The Voigt model unit, where η is the viscosity in the dashpot and M is the spring constant or elastic modulus.

For this model the strain has the same value at each element however the total stress of the model is the sum of the individual stresses. Therefore the stress-strain (σ - ϵ) relation for this model can be described by the equation

$$\sigma = M\epsilon + \eta\dot{\epsilon}, \quad (3.1)$$

where M is the spring constant or elastic modulus and η is the viscosity constant of the dashpot.

For the Maxwell model the viscous and elastic elements are arranged in series as can be seen in figure 3.2. The value of the stress is the same across each element and the total strain

is the sum of the individual strain of the elements. Therefore the stress-strain (σ - ϵ) relation can be described by the following equation for this model

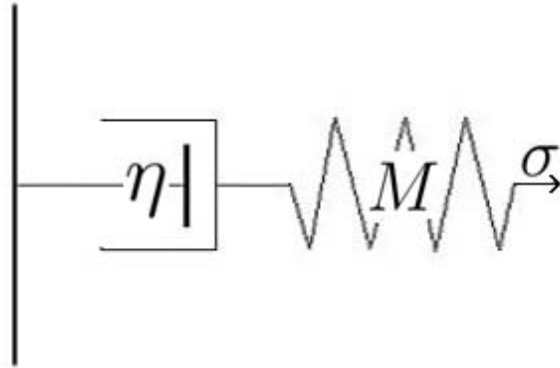


Figure 3.2: The Maxwell model unit, where η is the viscosity in the dashpot.

$$\sigma + (\eta/M)\dot{\sigma} = \eta\dot{\epsilon}. \quad (3.2)$$

In the Maxwell model when a stress is applied the spring suffers instantaneous strain due to the spring followed by linear viscous creep due to the dashpot. In Figure 3.3 the response of this system in time can be observed. The generalized stress-strain equation can be also be rewritten in terms of the relaxation time τ and the elastic constant M as (Nowick and Berry, 1972)

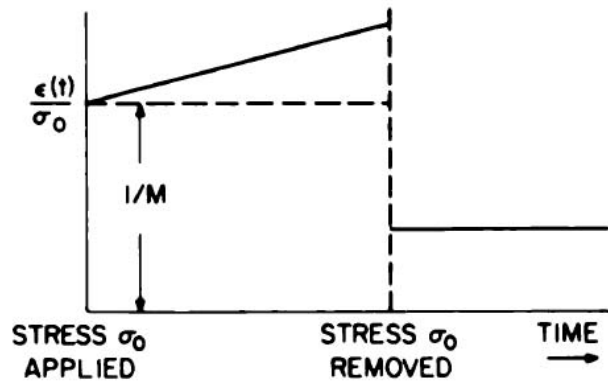


Figure 3.3: The Maxwell model unit response (Nowick and Berry, 1972)

$$\tau \dot{\sigma} + \sigma = \tau M \dot{\epsilon}. \quad (3.3)$$

This model however still does not display the recoverable creep characteristics of anelasticity. Therefore a spring in parallel must be introduced in the model in order for this simple system to display anelastic characteristics. This model is called a *Standard Linear Solid* or *SLS* for short. A more general model based on the *SLS* properties is called the generalized Maxwell model. A description and particularities of this model will be given in section 3.4.

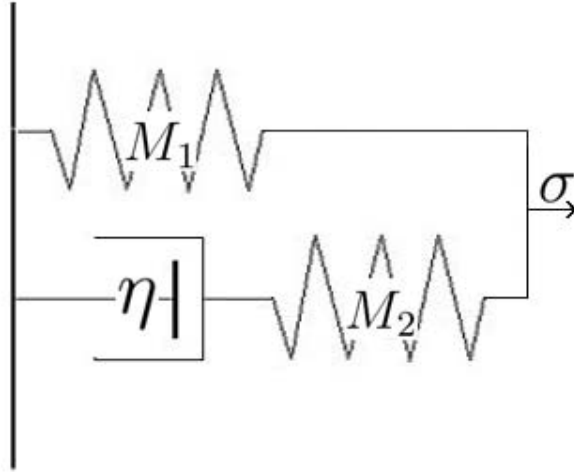


Figure 3.4: The *Standard Linear Solid* or *SLS*

3.3 STRAIN-STRESS RELATION FOR ANELASTIC MEDIA

In order to solve the problem of wave propagation through these models and obtain synthetic seismograms, the equation of motion must be solved numerically. This equation links the stress and the particle displacement in the medium and can be written in the form

$$\sigma_{ij,j} + f_i = \rho \ddot{u}_i, \quad (3.4)$$

where $i = 1, 2, 3$, σ_{ij} is the stress tensor, f_i is the body force, ρ is the density and u_i is the displacement, and where the summation convention is used (i.e., a doubly-repeated subscript

in a term indicates a sum over that subscript from 1 to 3). The “, j ” denotes means $\partial/\partial x_j$, and an overhead dot means $\partial/\partial t$.

The general linear constitutive relation for an isotropic medium in 1-D can be described by the following equation known as the Boltzmann’s superposition principle. (Christensen, 1971)

$$\sigma = \int_{-\infty}^t R(t - \tau)\dot{\epsilon}(\tau)d\tau, \quad (3.5)$$

which can be rewritten in its convolutional form

$$\sigma = R * \dot{\epsilon}, \quad (3.6)$$

or using the differentiation property of the convolution

$$\sigma = \dot{R} * \epsilon, \quad (3.7)$$

where σ is the stress. The integrating function R is the stress response to a unit step in strain and it is called the relaxation function. ϵ is the strain, $\epsilon = u'$ where u is the particle displacement and prime indicate partial differentiation with respect to space (x). Although all the functions involved in the aforementioned equation are functions of space and time we will only show in the following mathematical treatment the time dependence in the notation. Equation (3.5) relates the dependence of the stress at any given time to the weighted increments of strain ϵ . The stress history is a function of the relaxation function in the material and therefore depends on the superposition of the strain at previous times (Carcione et al., 1988). $R(t)$ can be written according to the following expression

$$R(t) = [M_R + \delta M\phi(t)]H(t), \quad \delta M = M_U - M_R, \quad (3.8)$$

where the constants M_U and M_R are the un-relaxed and the relaxed elastic modulus and represents the value of the ratio of stress to strain before and after relaxation of the system

(Liu et al., 1976). δM is the relaxation of the modulus and ϕ is a certain function of time that will be described ahead in this chapter. The function $H(t)$ is the well known Heaviside function. If the material has an anelastic response then $M_R > 0$ (Day and Minster, 1984). The function $R(t)$ is related to the viscoelastic modulus $M(t)$ by the following expression

$$M(t) = \frac{dR(t)}{dt}. \quad (3.9)$$

Equation (3.5), or (3.6), can be written in the frequency domain as

$$\bar{\sigma}(\omega) = \bar{M}(\omega)\bar{\epsilon}(\omega), \quad (3.10)$$

where $\bar{M}(\omega)$ is the complex viscoelastic modulus, and where the overhead bar indicates a Fourier time transform.

Equation (3.5) is very important in the description of the physical meaning of linear viscoelasticity since it shows that the stress at time t is related to the previous strain history and the function M which is characteristic of the material. Therefore samples under a set of finite strains show a *memory* of past values that also depends on internal values of the material. Therefore to solve the problem of anelasticity these equations must be discretized and time stepped in order to simulate the propagation of waves in viscoelastic media.

3.4 THE EK METHOD

One of the earliest attempts to solve the problem of anelasticity can be found in an article by Day and Minster published in 1984. In their paper "Numerical simulation of attenuated wavefields using a Padé approximant method" they transform the convolution integral given by equation (3.5) into a sequence of differential operators of increasing order that incorporates constant coefficients. Day and Minster obtained the following equation for the stress-strain

relation.

$$\sigma(t) = M_U \left[\epsilon(t) - \sum_{j=1}^n \zeta_j(t) \right], \quad (3.11)$$

where M_U is the un-relaxed modulus and where the "internal" or "memory variables" ζ_j can be calculated solving the following n first order differential equations

$$\dot{\zeta}_j(t) + v_j \zeta_j(t) = \lambda_j \frac{\delta M}{M_U} \epsilon(t), \quad j = 1 \dots n, \quad (3.12)$$

where λ_j and v_j are the residues and zeros of a set of orthonormal polynomials p_n used to build the Padé approximant for the operational modulus \bar{M} in the equation $\bar{\sigma}(s) = \bar{M}(s)\bar{\epsilon}(s)$.

The work by Day and Minster on the transformation of the frequency-dependent viscoelastic modulus into a rational function gives very good results when few coefficients are calculated. However for strong attenuation and longer travel paths the results were unsatisfactory. In addition the coefficients are found analytically and do not have a physical meaning (Emmerich and Korn, 1987).

Based on the limitations of the Day and Minster approach Emmerich and Korn proposed a method to approximate the viscoelastic modulus based on the rheology of the generalized Maxwell body. This model, which is also known as the Maxwell-Wiechert model, consist in a combination of a spring in parallel with a series of springs and dashpots containing an ideal viscous liquid also known as Maxwell unit or model. In figure 3.5 we can observe how the generalized Maxwell body is composed by the addition of Maxwell units in parallel to an elastic element. One of the advantages of this method is its straightforward implementation capabilities in a finite difference formulation.

In the generalized Maxwell model in its simplest case, namely the *Standard Linear Solid*, all four parameters σ , $\dot{\sigma}$, ϵ , $\dot{\epsilon}$ appear in the stress-strain relation. The governing equation can be written in terms of the relaxed (M_R), unrelaxed (M_U) modulus and the stress relaxation

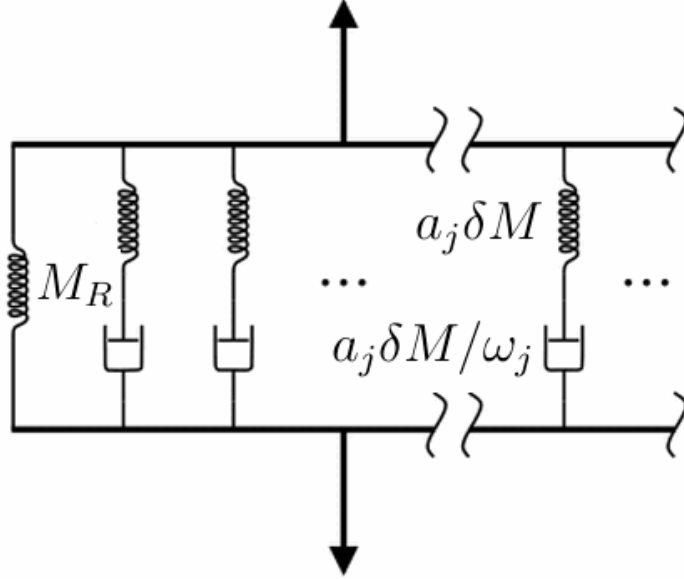


Figure 3.5: The generalized Maxwell body or Maxwell-Wiechert model. In the figure the elastic moduli and viscosities are represented by springs and dashpots respectively.

time τ_σ

$$\sigma + \tau_\sigma \dot{\sigma} = M_R \epsilon + \tau_\sigma M_U \dot{\epsilon}. \quad (3.13)$$

From the previous equation and assuming a unit step function in stress ($\sigma = H(t)$) we can obtain the creep function $c(t)$ which is the strain produced by step function in stress

$$c(t) = \frac{1}{M_R} \left[1 - \left(1 - \frac{M_R}{M_U} \right) \exp(-t/\tau_\epsilon) \right] H(t), \quad (3.14)$$

where in the aforementioned equation τ_ϵ is the strain relaxation time under constant stress. Similarly, the stress for a unit step function in strain $R(t)$, which is the relaxation function, is given by

$$R(t) = M_R \left[1 + \left(\frac{M_U}{M_R} - 1 \right) \exp(-t/\tau_\sigma) \right] H(t). \quad (3.15)$$

where τ_σ is the stress relaxation time under constant strain. A superposition of such exponentials can be used to obtain the generalized Maxwell model. For this case the relaxation

function $R(t)$ can be written in the form

$$R(t) = \left[M_R + \delta M \int_0^\infty r(\omega') \exp(-\omega' t) d\omega' \right] H(t), \quad (3.16)$$

where $\int_0^\infty r(\omega') \exp(-\omega' t) d\omega' = \phi(t)$ in equation (3.8) and where $M_R = \lim_{t \rightarrow \infty} M(t)$ is the relaxed modulus and $r(\omega)$ is the normalized relaxation spectrum that must satisfy the following equation so that $R(0) = M_U$

$$\int_0^\infty r(\omega') d\omega' = 1. \quad (3.17)$$

Using equation (3.16), it can be seen that the unrelaxed modulus is given by

$$M_U = \lim_{t \rightarrow 0} R(t) = M_R + \delta M. \quad (3.18)$$

In figure 3.6 the shape of a relaxation function is displayed. A sudden load of strain is characterized by the unrelaxed state of the relaxation function. With time the stress decays asymptotically assuming that the deformation is kept constant. The function $R(t)$ describes the material properties of the medium and makes the stress to depend less on recent values of the strain. In other words the viscoelastic material has a *fading memory* of the history of strain.

One assumption made is that the spectrum of the relaxation function is formed by J peaks of strength a_j at discrete relaxation frequencies ω_j

$$r(\omega) = \sum_{j=1}^J a_j \delta(\omega - \omega_j), \quad (3.19)$$

with

$$\sum_{j=1}^J a_j = 1, \quad (3.20)$$

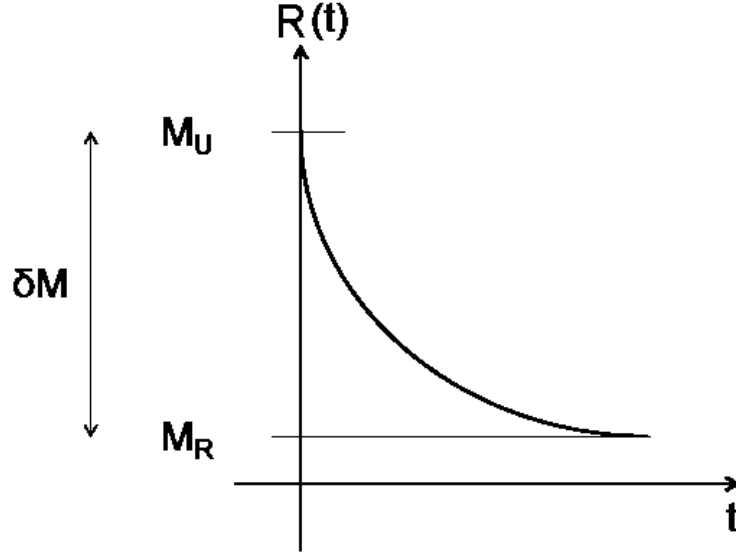


Figure 3.6: The relaxation function represented as an exponential decay function. The subscripts "U" and "R" indicate unrelaxed and relaxed respectively

and substituting (3.19) in (3.16) the following discrete expression for the relaxation function can be obtained

$$R(t) = \left[M_R + \delta M \sum_{j=1}^J a_j \exp(-\omega_j t) \right] H(t). \quad (3.21)$$

Equation (3.7) can be written in the following integral form

$$\sigma(t) = \int_{-\infty}^t \dot{R}(t - \tau) \epsilon(\tau) d\tau, \quad (3.22)$$

and differentiating $R(t)$ we obtain

$$\dot{R}(t) = M_R \delta(t) + \delta M \sum_{j=1}^J a_j [\exp(-\omega_j t) \delta(t) - \omega_j \exp(-\omega_j t) H(t)]. \quad (3.23)$$

Substituting (3.23) into equation (3.22) we can obtain

$$\sigma(t) = \int_{-\infty}^t M_R \delta(t - \tau) \epsilon(\tau) d\tau + \delta M \sum_{j=1}^J a_j \left[\int_{-\infty}^t \exp[-\omega_j(t - \tau)] \delta(t - \tau) \epsilon(\tau) d\tau \right. \\ \left. - \omega_j \int_{-\infty}^t \exp[-\omega_j(t - \tau)] H(t - \tau) \epsilon(\tau) d\tau \right], \quad (3.24)$$

where it is not difficult to see that

$$\int_{-\infty}^t M_R \delta(t - \tau) \epsilon(\tau) d\tau = M_R \epsilon(t), \quad (3.25)$$

$$\int_{-\infty}^t \exp(-\omega_j(t - \tau)) \delta(t - \tau) \epsilon(\tau) d\tau = \epsilon(t), \quad (3.26)$$

and using the fact that $M_R = M_U - \delta M$ and $\sum_{j=1}^J a_j = 1$ we can write

$$\sigma(t) = M_U \epsilon(t) - \delta M \epsilon(t) + \delta M \epsilon(t) - \delta M \sum_{j=1}^J a_j \omega_j \int_{-\infty}^t \exp[-\omega_j(t - \tau)] \epsilon(\tau) d\tau, \quad (3.27)$$

where taking M_U as common factor and moving $\frac{\delta M}{M_U}$ inside the sum we finally obtain

$$\sigma(t) = M_U \left[\epsilon(t) - \sum_{j=1}^J \zeta_j(t) \right]. \quad (3.28)$$

Variables ζ_j are defined by the following expression

$$\zeta_j = a_j \omega_j \frac{\delta M}{M_U} \int_{-\infty}^t \exp[-\omega_j(t - \tau)] \epsilon(\tau) d\tau. \quad (3.29)$$

In equation (3.28) we can see the stress expressed as a function of an elastic and anelastic terms involving the functions ζ_j

By applying the Leibniz differentiation rule to (3.29) and evaluating terms the following equation can be obtained

$$\dot{\zeta}_j(t) = a_j \omega_j \frac{\delta M}{M_U} \left[\int_{-\infty}^t (-\omega_j) \exp[-\omega_j(t - \tau)] \epsilon(\tau) d\tau - 0 + \epsilon(t) \right], \quad (3.30)$$

and after rearranging terms

$$\dot{\zeta}_j(t) + \omega_j \zeta_j(t) = a_j \omega_j \frac{\delta M}{M_U} \epsilon(t). \quad (3.31)$$

Applying the Fourier transform to $\dot{R}(t)$ in equation (3.23) and using equation (3.9) yields the following equation after some work

$$\bar{M}(\omega) = M_R + \delta M \sum_{j=1}^J \frac{i\omega a_j}{i\omega + \omega_j}. \quad (3.32)$$

This equation represents in the frequency domain the rheological model of the generalized Maxwell body. The constant M_R represents the effect of the elastic element in the model. The terms $a_j\delta M/\omega_j$ represents the viscosity and $a_j\delta M$ is the elastic modulus that characterize the Maxwell unit. In figure 3.7 we can see the elements of the generalized Maxwell body. A time marching finite difference code implementation is straightforward given that we now have a first order differential equation for the "memory variables" and the resulting equation of motion, that can be solved via a finite difference scheme.

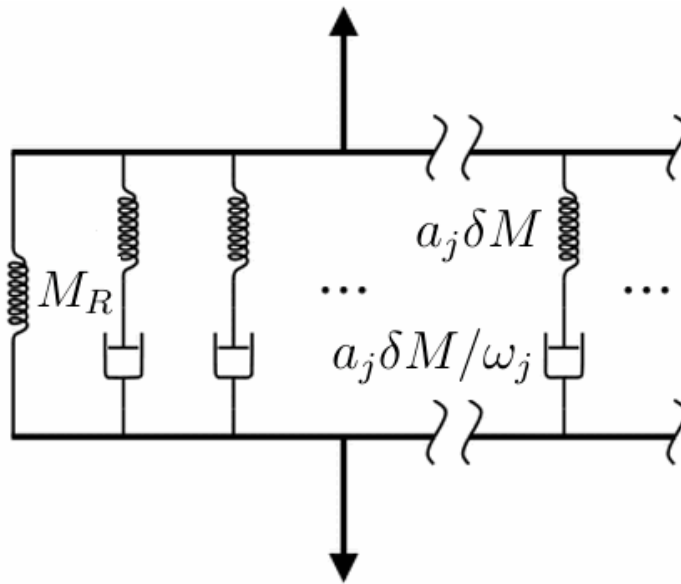


Figure 3.7: The generalized Maxwell body or Maxwell-Wiechert model. In the figure the elastic moduli and viscosities are represented by springs and dashpots respectively.

3.5 FINITE DIFFERENCE IMPLEMENTATION OF ANELASTIC WAVE MODELING

Given the aforementioned advantages of the Emmerich and Korn implementation of the rheological model of the generalized Maxwell body it is convenient to find a straight forward finite difference implementation to numerically solve this problem. Their starting point is the assumption of a homogeneous medium where M_U and M_R are constants. Substituting equation (3.28) into the stress-strain relation for a 1D anelastic medium

$$\rho \ddot{u} = \sigma', \quad (3.33)$$

where σ primed is the partial differentiation of the stress with respect to space. The following hyperbolic differential equation can be obtained

$$\ddot{u} = \beta^2 \left[u'' - \sum_j \xi_j \right], \quad (3.34)$$

where $\xi_j \equiv \zeta'_j$ and $\beta = \sqrt{M_U/\rho}$ is the elastic wave velocity also known as the unrelaxed wave velocity. In this equation \ddot{u} and u'' represents the second temporal and spatial derivatives of the displacement respectively. ξ satisfies then the differential equation

$$\dot{\xi}_j(t) + \omega_j \xi_j(t) = a_j \omega_j \frac{\delta M}{M_U} u''. \quad (3.35)$$

In order to make discrete the continuous variables both temporal and spatial as well as the equations we make $z = nh$ and $t = q\Delta t$. Where h and Δt are the spatial and temporal steps.

A second order discretization of equation (3.35) using standard central differences yield the following result

$$\frac{\xi_{j,n}^{q+1/2} - \xi_{j,n}^{q-1/2}}{\Delta t} + \omega_j \frac{\xi_{j,n}^{q+1/2} + \xi_{j,n}^{q-1/2}}{2} = a_j \omega_j \frac{\delta M}{M_U} (u'')_n^q, \quad (3.36)$$

where the average is taken in the second term on the left for numerical stability. Solving for $\xi_{j,n}^{q+1/2}$ gives

$$\xi_{j,n}^{q+1/2} = A_j \xi_{j,n}^{q-1/2} + B_j (u''_n)^q, \quad (3.37)$$

where $A_j = (2 - \omega_j \Delta t)/(2 + \omega_j \Delta t)$ and $B_j = \frac{2a_j \omega_j \Delta t}{(2 + \omega_j \Delta t)} \frac{\delta M}{M_U}$

As for equation (3.34) we can obtain the following formula for the homogeneous anelastic case

$$u_n^{q+1} = 2u_n^q - u_n^{q-1} + p^2 \left[u_{n+1}^q - 2u_n^q + u_{n-1}^q - \frac{h^2}{2} \sum_j (\xi_{j,n}^{q+1/2} + \xi_{j,n}^{q-1/2}) \right], \quad (3.38)$$

where the scheme is stable if the condition $\beta \Delta t/h \leq 1/\sqrt{2}$ is met and $p = \sqrt{M_U/\rho}(\Delta t/h)$

Korn and Stöckl proposed a method to obtain an equation equivalent for the heterogeneous case by generalizing the spatial derivatives in the wave equation for the elastic case using the fictitious points. Emmerich and Korn obtained an operator as a result of the application of the fictitious points scheme to solve boundary conditions. The heterogeneous formulation of the anelastic case then becomes

$$u_n^{q+1} = 2u_n^q - u_n^{q-1} + 2p^2 \left[C_n - \frac{h^2}{4} \sum_j (\xi_{j,n}^{q+1/2} + \xi_{j,n}^{q-1/2}) \right], \quad (3.39)$$

and

$$\xi_{j,n}^{q+1/2} = A_j \xi_{j,n}^{q-1/2} + 2B_j C_n/h^2, \quad (3.40)$$

where

$$C_n = \frac{M_{U,n+1}}{M_{U,n+1} + M_{U,n}} (u_{n+1}^q - u_n^q) - \frac{M_{U,n-1}}{M_{U,n-1} + M_{U,n}} (u_n^q - u_{n-1}^q). \quad (3.41)$$

Quiroga-Goode and Krebes proposed a solution based on the application of a central difference operator consecutively applied to the right-hand side of equation (3.33) (Krebes

and Quiroga-Goode, 1994). This method yield a stable heterogeneous formulation that is easier to conceptually understand and implement than the EK method. To develop this scheme Krebs and Quiroga-Goode started by approximating equations (3.28), (3.31) and (3.33) in the form

$$\sigma_n^q = M_U \left[\frac{1}{h}(u_{n+1}^q - u_{n-1}^q) - \sum_{j=1}^J \zeta_{j,n}^q \right], \quad (3.42)$$

$$\frac{1}{\Delta t}(\zeta_{j,n}^{q+1/2} - \zeta_{j,n}^{q-1/2}) + \frac{\omega_j}{2}(\zeta_{j,n}^{q+1/2} + \zeta_{j,n}^{q-1/2}) = a_j \omega_j \frac{(\delta M)_n}{h M_{U,n}} (u_{n+1/2}^q - u_{n-1/2}^q), \quad (3.43)$$

$$\frac{\rho_n}{(\Delta t)^2} [u_n^{q+1} - 2u_n^q + u_n^{q-1}] = \frac{1}{h} (\sigma_{n+1/2}^q - \sigma_{n-1/2}^q), \quad (3.44)$$

respectively.

Then substituting equation (3.42) into (3.44) we obtain

$$u_n^{q+1} = 2u_n^q - u_n^{q-1} + \frac{1}{\rho_n} \left(\frac{\Delta t}{h} \right)^2 \left(M_{U,n+1/2} \left[u_{n+1}^q - u_n^q - \frac{h}{2} \sum_j (\zeta_{j,n+1/2}^{q+1/2} + \zeta_{j,n+1/2}^{q-1/2}) \right] - M_{U,n-1/2} \left[u_n^q - u_{n-1}^q - \frac{h}{2} \sum_j (\zeta_{j,n-1/2}^{q+1/2} + \zeta_{j,n-1/2}^{q-1/2}) \right] \right), \quad (3.45)$$

with

$$\zeta_{j,n+1/2}^{q+1/2} = A_j \zeta_{j,n+1/2}^{q-1/2} + B_{j,n+1/2} (u_{n+1}^q - u_n^q) / h, \quad (3.46)$$

and where we have use the fact that $\zeta_{j,n+1/2}^q = \frac{1}{2}(\zeta_{j,n+1/2}^{q+1/2} + \zeta_{j,n+1/2}^{q-1/2})$.

In order to evolve the system in time the $4J$ first order differential equations (3.31) for ζ must be solved in addition to the hyperbolic second order differential equation (3.28). This scheme based on the consecutive applications of the central difference operators to the equation of motion for a heterogeneous medium is called the standard scheme (Krebs and

Quiroga-Goode, 1994). One interesting analysis of the comparison of the Emmerich and Korn and the present formulations is the homogeneous case. For this case the standard scheme formula (3.45) can be rewritten as

$$u_n^{q+1} = 2u_n^q - u_n^{q-1} + \frac{M_U}{\rho_n} \left(\frac{\Delta t}{h} \right)^2 \left(u_{n+1}^q - 2u_n^q + u_{n-1}^q - \frac{h}{2} \sum_j (\zeta_{j,n+1/2}^{q+1/2} + \zeta_{n+1/2}^{q-1/2}) - \frac{h}{2} \sum_j (\zeta_{j,n-1/2}^{q+1/2} + \zeta_{j,n-1/2}^{q-1/2}) \right) \quad (3.47)$$

Equation (3.47) is equivalent to equation (3.38) if $\xi_{j,n}^{q+1/2} = (\zeta_{j,n+1/2}^{q+1/2} - \zeta_{j,n-1/2}^{q+1/2})/h$.

Therefore for the homogeneous case both formulations are equivalent taking into account that the aforementioned equation is the spatial central finite difference approximation for ξ at $t = (q + 1/2)\Delta t$.

In order to make a comparison between the EK and the standard method we created the model depicted in figure 3.8. In this model the receiver is represented by the triangle and the round symbol represents the source location. The offset between source and receiver is 500 meters. The selection of densities and velocities for the model does not necessarily represent a real scenario. The velocities are the un-relaxed velocities of a wave at infinite frequency. Since in our model the values of Q are nearly constant in a range of 0.02 to 20 Hz , the velocities of our model are calculated at the reference frequency of 20 Hz

As a source we use a pulse generated by the following equation $s(t) = c(\sin(2\pi f_p t) - 0.5\sin(4\pi f_p t))$ for $0 < t < 1/f_p$ and $s(t) = 0$ for all other t . In the equation $c = 1$ and $f_p = 10Hz$. In figure 3.9 we can a graph of the pulse for the selected parameters and its spectra.

As can be seen in figure 3.10, for the inhomogeneous case, both formulations yield almost identical results. In figure 3.11 we can see in more detail the reflection produced by the first interface. This zoomed section highlights the small difference between these methods.

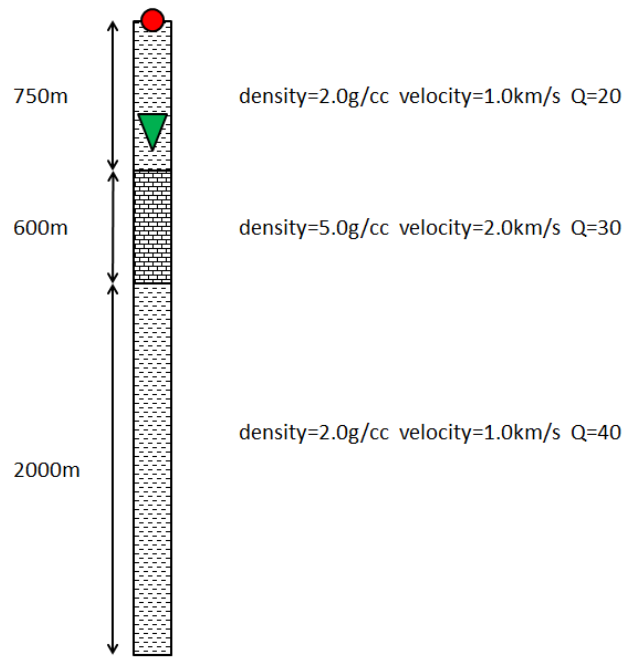


Figure 3.8: Problem geometry and model.

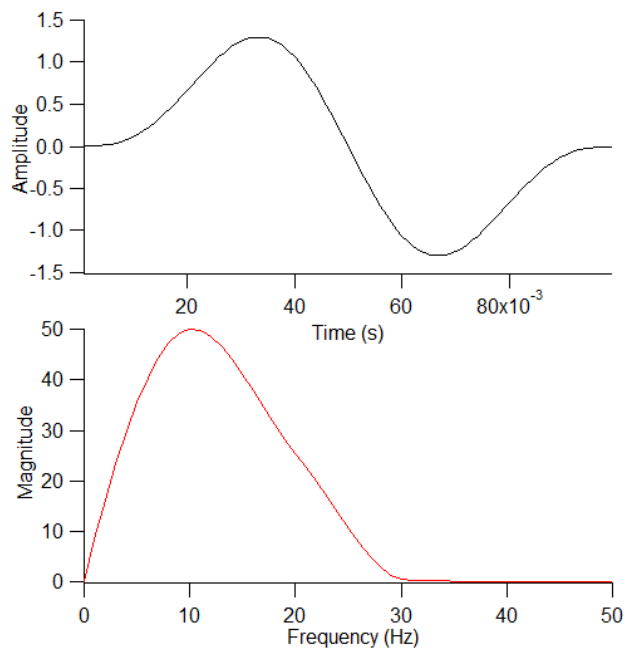


Figure 3.9: Top: Pulse used in the simulations. Bottom: Amplitude spectrum of the pulse.

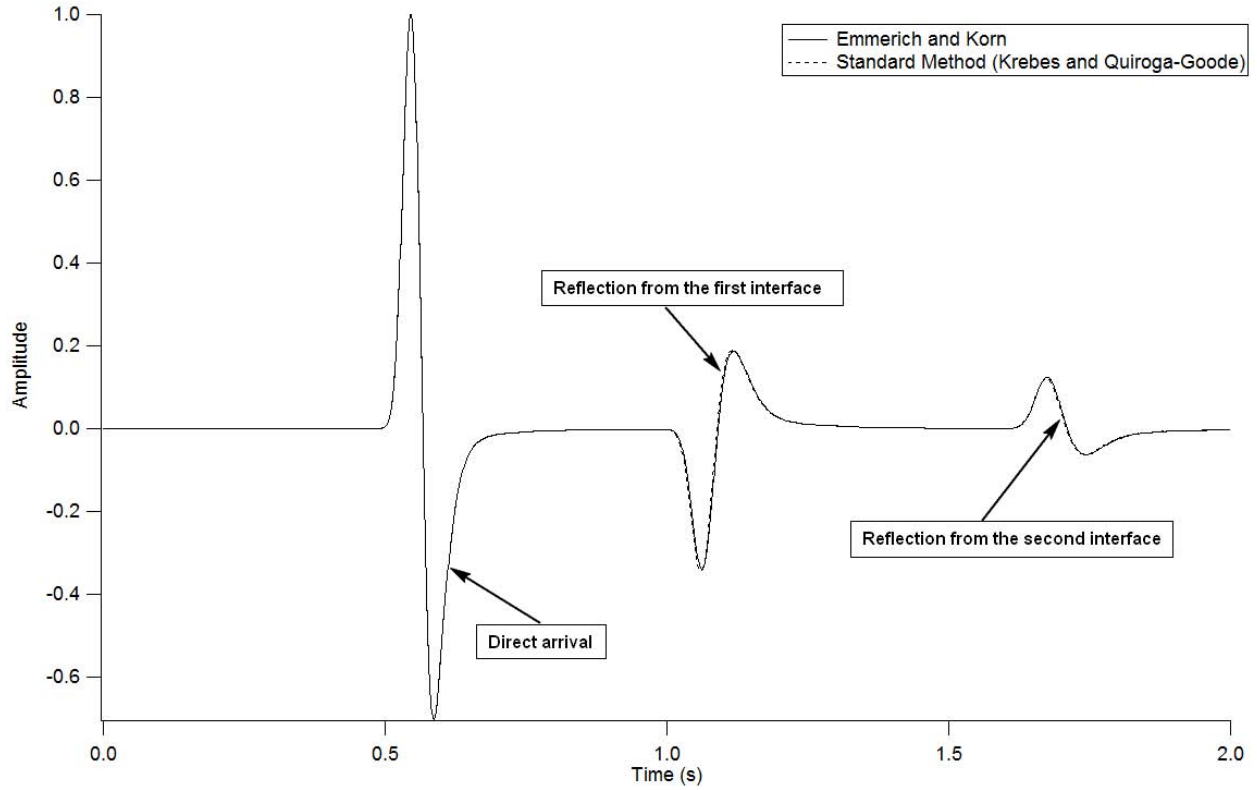


Figure 3.10: Comparison of the Emmerich and Korn method and the standard method proposed by Krebs and Quiroga-Goode

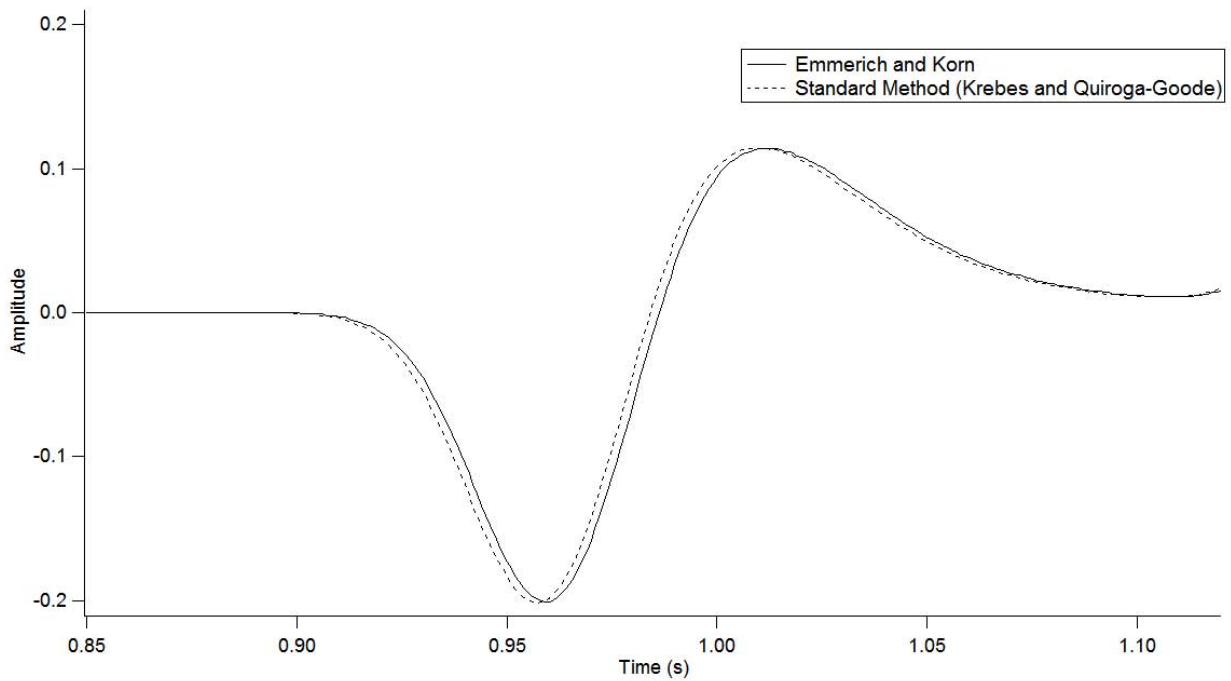


Figure 3.11: Comparison of the Emmerich and Korn method and the standard method proposed by Krebs and Quiroga-Goode. Detail of the reflection produced at the first interface.

Chapter 4

MODELING FRACTURES IN ANELASTIC ISOTROPIC MEDIA

4.1 INTRODUCTION

Finite difference modeling is one of the most popular and accurate tools for solving numerical problems in seismology. Numerical modeling is widely used to solve a large range of problems from structural analysis to inversion and migration of seismic data. The increase in computing power and ease of implementation allow one to solve problems with complex models and rheologies. Analytical methods on the other hand, although faster, are useful only for solving a handful of simple problems. Although the simplicity in both coding and usage of the finite difference method make it a preferred solution, special attention must be paid to the accuracy of the method in order to obtain physically correct results.

Finite difference methods can be grouped into two main categories: Explicit methods and implicit methods. In the implicit finite difference schemes more than one grid point can be found at the uppermost time level. On the other hand for the implicit methods only one of such points can be found at the uppermost time level (Krebes, 2010). In both cases the partial derivatives are replaced by approximations obtained by Taylor series near the point of interest. For example for the case of the forward finite difference approximation (FFDA) at the point x for a small Δx we can write $f(x + \Delta x) = f(x) + \frac{\partial f(x)}{\partial x} \Delta x + O((\Delta x)^2)$ therefore $\frac{\partial f(x)}{\partial x} \approx \frac{f(x+\Delta x) - f(x)}{\Delta x}$.

In addition to these two main categories there are two formulations of finite differences: the homogeneous and heterogeneous formulations. In the homogeneous formulation boundary conditions for every interface in the model must be satisfied explicitly, limiting the use

of the homogeneous formulation to simple geometries. Heterogeneous formulations are more advantageous to use because allows to assign a different acoustic property to every point in the grid (Carcione et al., 2002).

In this chapter we present a new method for solving the wave equation in order to simulate both the linear viscoelastic and the non-welded contact problem. We start from the work of (Krebes and Quiroga-Goode, 1994) and use the linear-slip boundary conditions proposed by (Schoenberg, 1980) to obtain a generalized homogeneous formulation to simulate propagation of the seismic wave through non-welded contact in anelastic media.

4.2 THE FICTITIOUS POINTS SCHEME APPLIED TO THE MODELING OF NON-WELDED CONTACT IN ANELASTIC MEDIA

Using the results from the literature presented above, I have formulated a theory of seismic modeling in media that encompasses both the anelastic wave propagation formulation as well as the treatment of the non-welded contact interfaces using finite differences. To the extent of our knowledge this approach using the fictitious point scheme to derive boundary conditions and its integration to a finite difference scheme has not been previously developed.

Let's write the boundary conditions for the non-welded contact in the form

$$(u_z^+)_{m+1/2} - (u_z^-)_{m+1/2} = \eta_N \sigma_{zz}, \quad (4.1)$$

$$(\sigma_{zz}^+)_{m+1/2} = (\sigma_{zz}^-)_{m+1/2}, \quad (4.2)$$

where u_z is the particle displacement on both sides of the boundary. + and - superscripts are used in these equations in order to distinguish from quantities on the positive ($z > z_{m+1/2}$) and negative side of the boundary ($z < z_{m+1/2}$). In the equation σ_{zz}^+ and σ_{zz}^- are the stresses on either side of the boundary. In figure 4.1 the locations of the displacements and stresses are represented for greater clarity.

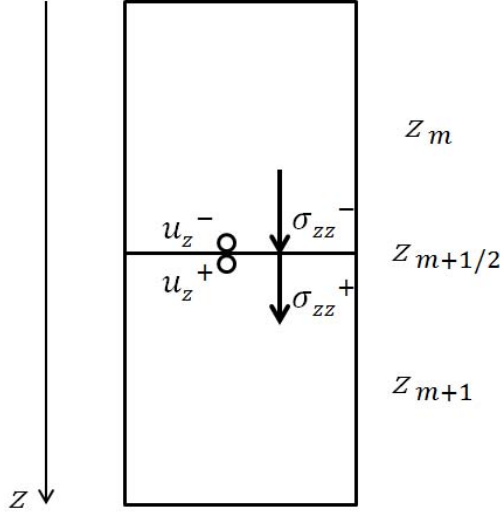


Figure 4.1: Schematic of the fictitious points scheme for the calculation of the non-welded contact. The circles represent the location of the displacements on both sides of the fracture while the arrows represents the stresses on both sides of the boundary.

We now extend the first medium by inserting an additional row into the second medium and vice-versa. The value of the amplitudes in the extended grids are the fictitious amplitudes. Using the average for the amplitudes and the centered difference operator for the stress the linear slip boundary conditions can be rewritten in terms of the fictitious points to $O(\Delta z)^2$ following a similar approach by Slawinski and Krebes (2002)

$$u_{m+1} + \tilde{u}_m - \tilde{u}_{m+1} - u_m = 2\eta_N M_U^+ \left[(1/h) (u_{m+1} - \tilde{u}_m) - \sum_j \zeta_j^+ \right], \quad (4.3)$$

$$M_U^+ \left[(1/h) (u_{m+1} - \tilde{u}_m) - \sum_j \zeta_j^+ \right] = M_U^- \left[(1/h) (\tilde{u}_{m+1} - u_m) - \sum_j \zeta_j^- \right], \quad (4.4)$$

where h is the spatial step size, u_m and \tilde{u}_m are the particle displacement at real and fictitious locations respectively, ζ_j are the memory variables and These equations are the extension of equations (2.8) and (2.9) to the non-welded contact case where memory variables have been included in the calculation of the stress to account for anelasticity. We can write the

aforementioned system of equations using matrices

$$\begin{bmatrix} 1 + 2\eta_N M_U^+ / h & -1 \\ M_U^+ / h & M_U^- / h \end{bmatrix} \begin{bmatrix} \tilde{u}_m \\ \tilde{u}_{m+1} \end{bmatrix} = \begin{bmatrix} \left(\frac{2\eta_N M_U^+}{h} - 1 \right) u_{m+1} + u_m - 2\eta_N M_U^+ Z^+ \\ (M_U^+ / h) u_{m+1} + (M_U^- / h) u_m - M_U^+ Z^+ + M_U^- Z^- \end{bmatrix}, \quad (4.5)$$

where we have made the change of variables $Z = \sum_j \zeta_j$ and solving for \tilde{u}_m and \tilde{u}_{m+1} we obtain

$$\tilde{u}_m = \frac{2hM_U^- u_m + hu_{m+1}(M_U^+ - M_U^-) + Z^- h^2 M_U^- - Z^+ h^2 M_U^+ + 2\eta_N M_U^+ M_U^- (u_{m+1} - hZ^+)}{hM_U^- + hM_U^+ + 2\eta_N M_U^+ M_U^-}, \quad (4.6)$$

$$\tilde{u}_{m+1} = \frac{2hM_U^+ u_{m+1} - hu_m(M_U^+ - M_U^-) + Z^- h^2 M_U^- - Z^+ h^2 M_U^+ + 2\eta_N M_U^+ M_U^- (u_m + hZ^-)}{hM_U^- + hM_U^+ + 2\eta_N M_U^+ M_U^-}. \quad (4.7)$$

We can use then the above results to implement the non-welded contact finite difference scheme by substituting the aforementioned values found for \tilde{u}_{m+1} and \tilde{u}_{m-1} in the equation of motion, where \tilde{u}_{m-1} obtained by substituting $m \rightarrow m - 1$ in \tilde{u}_m . Using equation (3.34) without considering the memory variables, as they have been considered in the treatment of boundary conditions, we can write

$$\ddot{u} = \beta^2 u''. \quad (4.8)$$

Using the standard method based on the application of the central difference operator we can obtain the following generalized homogeneous equation

$$\frac{\rho_m}{(\Delta t)^2} [u_m^{q+1} - 2u_m^q + u_m^{q-1}] = \frac{M_U}{h^2} [\tilde{u}_{m+1}^q - 2u_m^q + \tilde{u}_{m-1}^q], \quad (4.9)$$

and solving for u_m^{q+1}

$$u_m^{q+1} = 2u_m^q - u_m^{q-1} + \beta^2 \left(\frac{\Delta t}{h} \right)^2 [\tilde{u}_{m+1}^q - 2u_m^q + \tilde{u}_{m-1}^q], \quad (4.10)$$

where $\beta = \sqrt{M_U/\rho_m}$.

Therefore we can obtain a generalized homogeneous approach for the wave propagation in anelastic media considering the non-welded contact. In this approach a boundary with $\eta_N = 0$ will be in welded contact. In equation (4.10) we can substitute equations (4.6) and (4.7) making the change $m \rightarrow m - 1$ in equation (4.6). Hence we obtain

$$\begin{aligned} u_m^{q+1} = & 2u_m^q - u_m^{q-1} + \beta^2 \left(\frac{\Delta t}{h} \right)^2 \left[-2u_m^q \right. \\ & + \left(\frac{2hM_U^+ u_{m+1} - hu_m(M_U^+ - M_U^-) + Z^- h^2 M_U^- - Z^+ h^2 M_U^+ + 2\eta_N M_U^+ M_U^- (u_m + hZ^-)}{hM_U^- + hM_U^+ + 2\eta_N M_U^+ M_U^-} \right)_{m+1/2} \\ & \left. + \left(\frac{2hM_U^- u_{m-1} + hu_m(M_U^+ - M_U^-) + Z^- h^2 M_U^- - Z^+ h^2 M_U^+ + 2\eta_N M_U^+ M_U^- (u_m - hZ^+)}{hM_U^- + hM_U^+ + 2\eta_N M_U^+ M_U^-} \right)_{m-1/2} \right]. \end{aligned} \quad (4.11)$$

Let $(M_U^-)_{m-1/2} = M_{U,m-1}$, $(M_U^+)_{m-1/2} = M_{U,m}$, $(M_U^-)_{m+1/2} = M_{U,m}$ and $(M_U^+)_{m+1/2} = M_{U,m+1}$. In other words, the unrelaxed modulus and memory variables are evaluated at a cell and its adjacent ones on the FD stencil. This results in the following equation

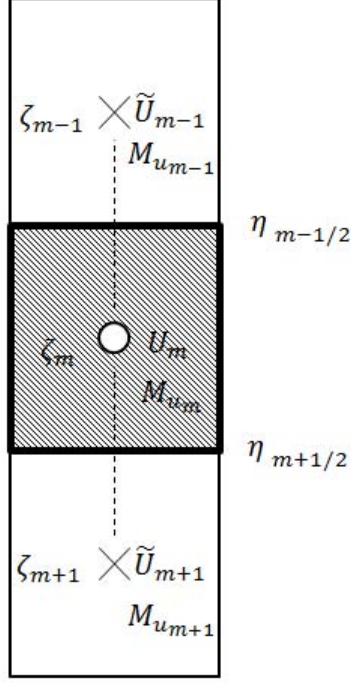


Figure 4.2: Stencil used in the formulation of the generalized homogeneous finite difference scheme.

$$\begin{aligned}
& u_m^{q+1} = 2u_m^q - u_m^{q-1} + \beta^2 \left(\frac{\Delta t}{h} \right)^2 \left[-2u_m^q \right. \\
& + \left(\frac{2hM_{U,m+1}u_{m+1} - hu_m(M_{U,m+1} - M_{U,m}) + Z_m h^2 M_{U,m} - Z_{m+1} h^2 M_{U,m+1}}{hM_{U,m} + hM_{U,m+1} + 2\eta_N M_{U,m+1} M_{U,m}} \right. \\
& \quad \left. + \frac{2\eta_N M_{U,m+1} M_{U,m} (u_m + hZ_m)}{hM_{U,m} + hM_{U,m+1} + 2\eta_N M_{U,m+1} M_{U,m}} \right) \\
& + \left(\frac{2hM_{U,m-1}u_{m-1} + hu_m(M_{U,m} - M_{U,m-1}) + Z_{m-1} h^2 M_{U,m-1} - Z_m h^2 M_{U,m}}{hM_{U,m-1} + hM_{U,m} + 2\eta_N M_{U,m} M_{U,m-1}} \right. \\
& \quad \left. + \frac{2\eta_N M_{U,m} M_{U,m-1} (u_m - hZ_m)}{hM_{U,m-1} + hM_{U,m} + 2\eta_N M_{U,m} M_{U,m-1}} \right) \left. \right]. \quad (4.12)
\end{aligned}$$

One difference with the standard method developed by Krebs and Quiroga-Goode is how memory variables are evaluated in the grid. As can be seen in the stencil, variables representing absorption are calculated at locations $m - 1$ and $m + 1$ unlike the STD method where the memory variables were calculated at locations $m + 1/2$ and $m - 1/2$.

Chapter 5

NUMERICAL SIMULATION OF NONWELDED CONTACT IN ANELASTIC ISOTROPIC MEDIA

5.1 INTRODUCTION

An attempt to model a system with a non-welded contact between anelastic-anelastic, elastic-anelastic and anelastic-elastic media is done in this chapter. The scheme developed is compared against the EK and standard schemes for the welded contact case. In the non-welded contact case the thickness of the fracture is negligible compared with the seismic wavelength. In this case is examined the impact of the value of the compliance or stiffness in the energy reflected and transmitted at the boundary.

Under laboratory conditions, the travel times and amplitudes of compressional and shear pulses have been measured while naturally fractured cylindrical rock specimens were subjected to a wide range of stresses up to $85MPa$ (Pyrak-Nolte et al., 1990). These measurements by Pyrak-Nolte showed, by measuring the differences in spectral amplitudes between pulses, that fractures filter out the high frequency components of the wave and introduce a time delay (Pyrak-Nolte et al., 1990), (Pyrak-Nolte, 1988). Both of these effects are also present in results of anelastic wave modeling. It is therefore of interest to assess how similar are these effects and what is the combined effect of a non-welded interface placed between two anelastic media on the wave propagation.

5.2 DESCRIPTION OF THE NUMERICAL MODEL

The numerical results in this section have been obtained using a modification of the algorithm developed by Krebes and Quiroga-Goode (1994) where we have included the calculation

of the amplitudes using the fictitious points scheme. An additional grid with values of compliance was added to the algorithm and the equation of motion is solved using equation (4.12). In figure 5.1 the geometry used in the numerical simulations can be appreciated. The first and third layers have the same densities and velocities while the intermediate layer presents both a velocity as well as density increase. An increase from $2g/cc$ to $5g/cc$ in the values of density is a large increase. Such variations in density are unlikely to occur in nature. The value selected for Q was 20, 30 and 40 respectively for the layered medium from top to bottom. The round symbol represents the source location and the triangle represent the receiver location in the model. The offset between source and receiver is 500 meters. As a source we use a pulse generated by the following equation (Emmerich and Korn, 1987)

$$s(t) = c(\sin(2\pi f_p t) - 0.5\sin(4\pi f_p t)), \quad 0 < t < \frac{1}{f_p}, \quad (5.1)$$

where $c = 1$ and $f_p = 10Hz$ and $s(t) = 0$ for all other t . In figure 5.2 both the shape of the pulse and the frequency spectrum are represented. The frequency spectrum extends up to $30Hz$. Figure 5.2 also shows that the spectrum of the time function displays a short tail beyond $30Hz$. This characteristic of the pulse effectively reduce grid dispersion in the FD method. This type of numerical noise is directly related to the grid spacing and affects the accuracy of the method. The cause behind this numerical problem is the propagation of high-frequency waves with a different velocity from true velocity in the model (Basabe and Sen, 2007).

I compared the results obtained with the developed method in this work for the welded contact case ($\eta_N = 0$) with results derived from the algorithms developed by Krebes and Quiroga-Goode and Emmerich and Korn. Hereinafter I will also refer to the finite difference scheme developed by Krebes and Quiroga-Goode as the standard method and to the Emmerich and Korn method as the EK method. Distance units in the code are given in km , density in $g * cm^{-3}$, velocity in $km * s^{-1}$. The spatial step size $h=0.0025km$ and time step

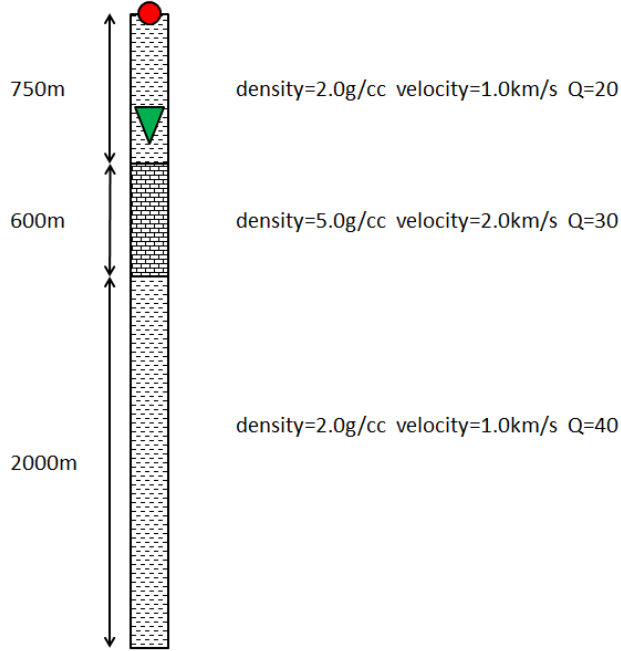


Figure 5.1: Problem geometry and model used in the numerical simulations.

size $\Delta t=0.001s$ resulting in a Courant number $p = \sqrt{2}\Delta t\beta/h \approx 1$. The spatial step size was calculated by using the following equation given by (Moczo, 1989)

$$h = \frac{c_{min}}{Wf_{max}}, \quad (5.2)$$

where W is the minimum number of points per smallest wavelength present in the model, c_{min} is the minimum velocity of the model and f_{max} is the maximum frequency of the source. The values of W is chosen usually to be 10 points however in our example we chose 13.33. For the welded contact case the value of the compliance $\eta_N = 0$ and therefore we expect the generalized homogeneous scheme developed in this work to be almost identical to the EK method and the standard method.

In figure 5.3 we can appreciate the result of the comparison of the standard, the EK and the method proposed in this work. In the seismogram we can appreciate three main events. From left to right we can observe the direct and the reflected waves coming from the first and second interface. The geometry of the simulation was chosen specifically to avoid

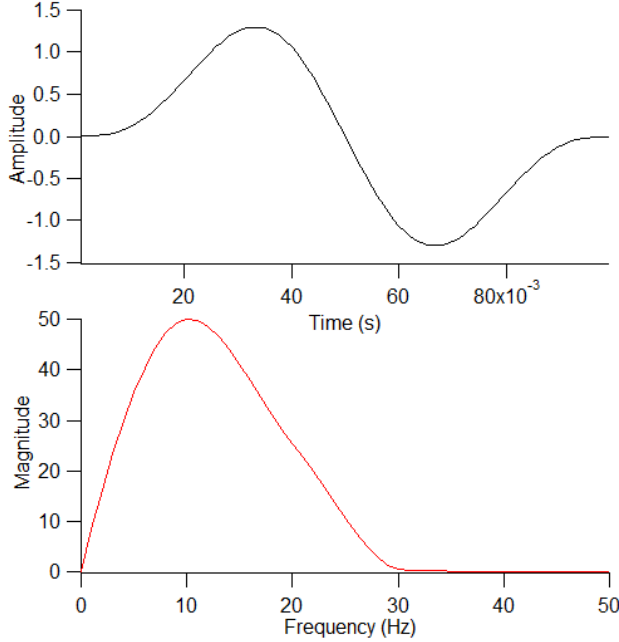


Figure 5.2: Top: Pulse used in the simulations. Bottom: Amplitude spectrum of the pulse.

multiple reflections coming from the interface located between the first and second media, as well as free surface reflections coming from the edge of the numerical grid. Reflections arriving from the first and second interfaces have opposite polarity given the low to high and subsequently high to low impedance contrast respectively. In the figure we can also appreciate that there are small differences between the three methods. At this scale the aforementioned difference is barely perceptible. In figures 5.4 and 5.5 we appreciate with more detail reflections coming from the first and second boundary. In these two images the difference among the three methods can be seen more easily.

In addition we also calculated the difference between our method and the standard method and between our method and the EK method in the case of welded contact. In addition the absolute value of the difference was also computed. The results show a very good agreement with the previous methods developed by Emmerich and Korn and Krebs and Quiroga-Goode. In figures 5.6 and 5.7 we can appreciate that the magnitude of the difference is not higher than 3%

The proposed method can also be compared with an analytical solution in order to verify

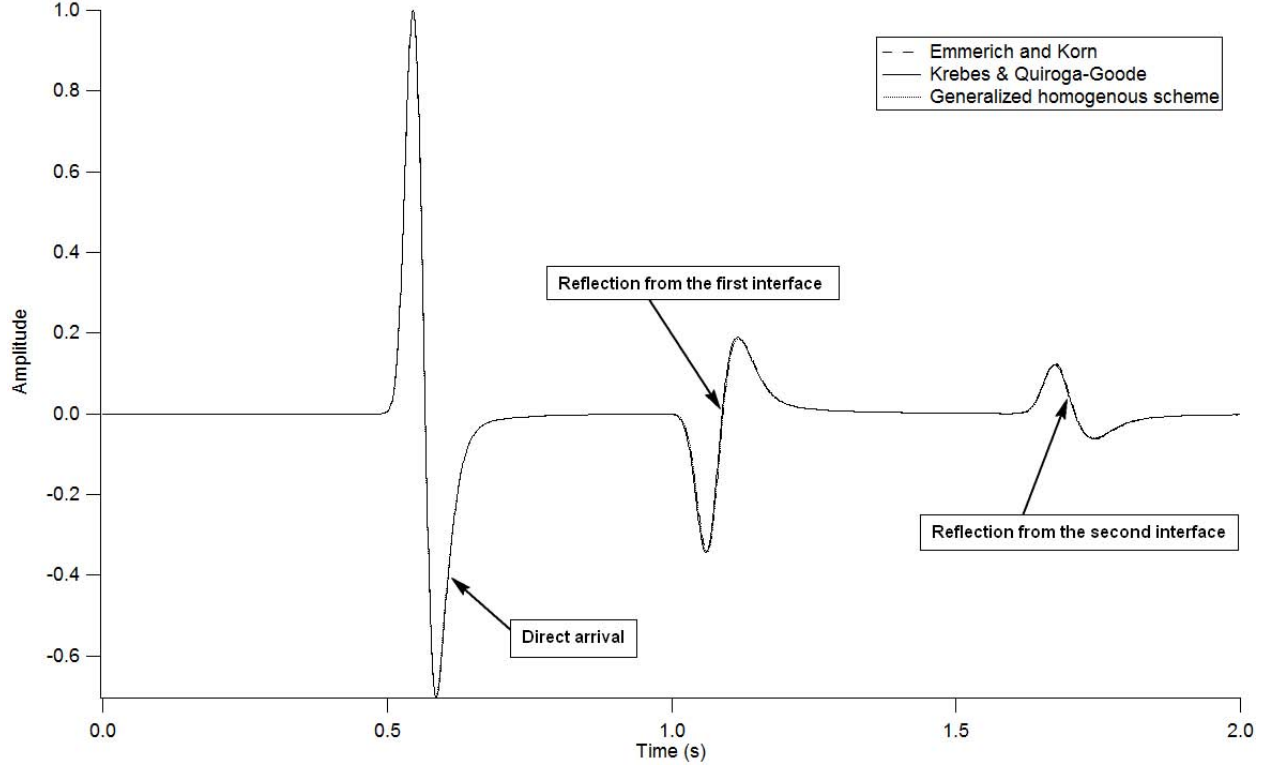


Figure 5.3: Comparison of the three methods with $\eta_N = 0$ (welded contact case). All graphs are normalized to a maximum amplitude of unity.

the accuracy of the proposed methodology. This allow us to test the accuracy of the method. In this work we use a ray tracing method called the *stationary ray* method (Slawinski and Krebs, 1991). In this method the solution of the Sommerfeld integral over the ray parameter for the wavefield at the receiver is an equation which, when solved, yields a complex-valued ray parameter, which corresponds to an incident inhomogeneous wave traveling at an oblique angle, i.e., as a body wave. (Slawinski and Krebs, 1991)

In this method the wavefield at the receiver can be calculated as a superposition of general plane waves of the form

$$\exp[i\omega(\tau - t)], \quad (5.3)$$

where $\omega = 2\pi f$ is the angular frequency. τ is the complex travelttime that can be calculated

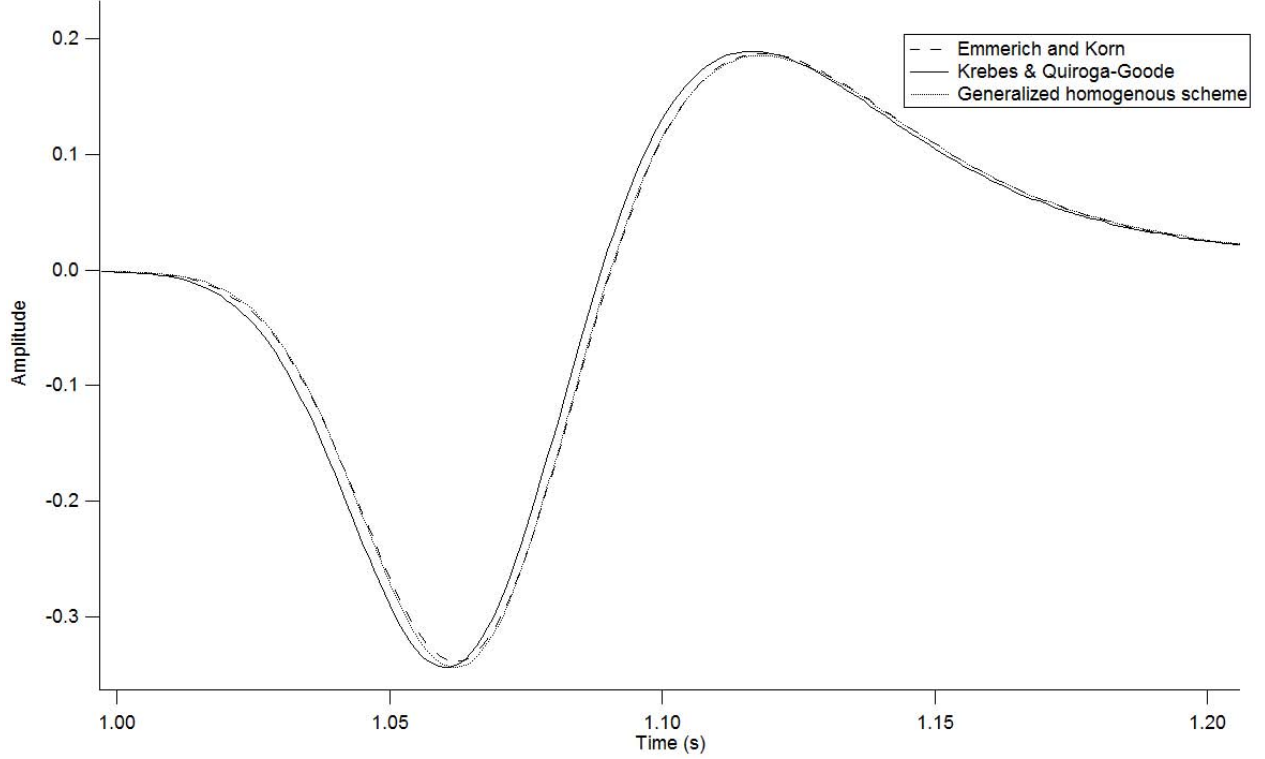


Figure 5.4: Comparison of the three methods with $\eta_N = 0$ (welded contact case). Detail of the first reflection. All graphs are normalized to a maximum amplitude of unity.

with

$$\tau = pX + \sum_{j=1}^m h_j \sqrt{v_j^{-2} - p^2}, \quad (5.4)$$

where p is the complex ray parameter, v_j is the complex wave speed associated with the j th ray and h_j is the vertical distance between beginning and end points of the j th ray segment (Slawinski and Krebes, 1991). The complex velocity formula is given by

$$v^2 = V^2 \left[\frac{1 + \sqrt{1 + Q^{-2}}}{2(1 + Q^{-2})} \right] (1 - iQ^{-1}), \quad (5.5)$$

for any Q and where, in this 1D case, V is the real-valued phase velocity of homogeneous plane waves (Slawinski and Krebes, 1991) i.e., waves for which the propagation and absorption vectors are parallel (see eq. 5.7 below). It is not difficult to see that for $Q \gg 1$ (5.5) is

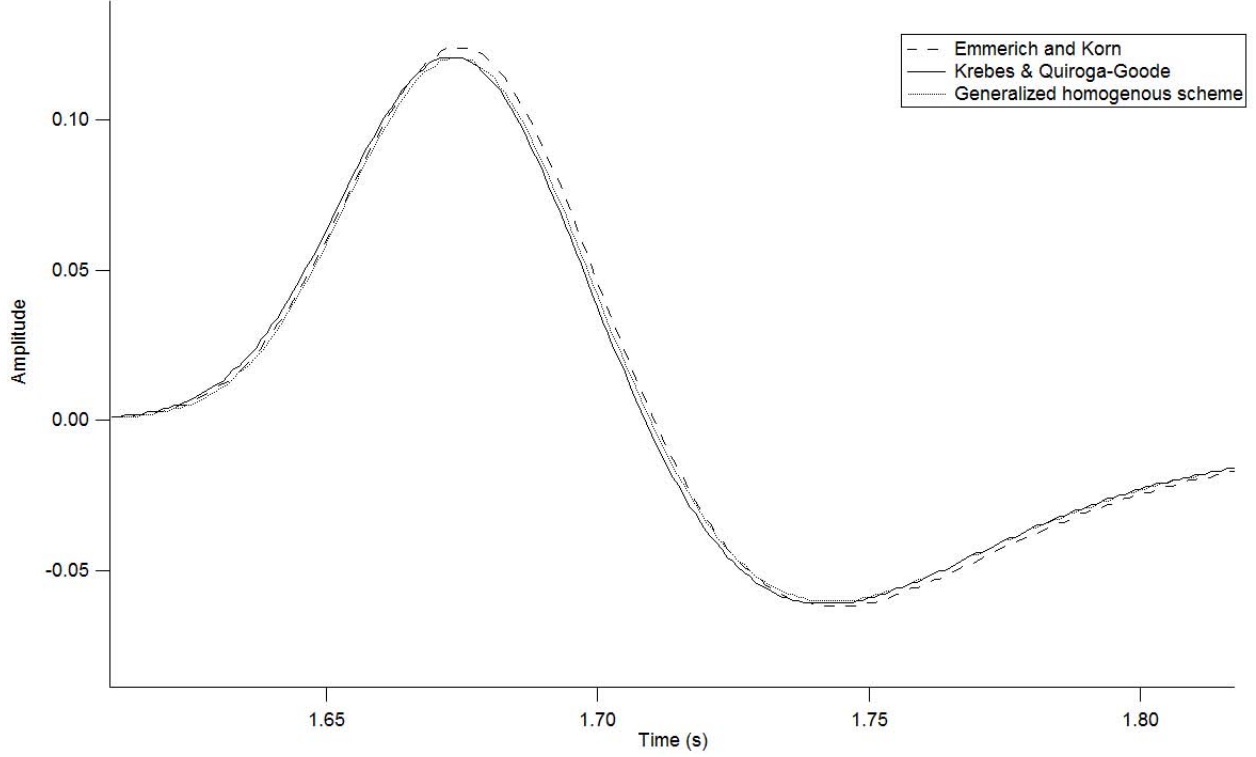


Figure 5.5: Comparison of the three methods with $\eta_N = 0$ (welded contact case). Detail of the second reflection. All graphs are normalized to a maximum amplitude of unity.

reduced to

$$v^2 = V^2(1 - iQ^{-1}). \quad (5.6)$$

For any given ray segment we can write

$$\exp[i(\mathbf{k} \cdot \mathbf{x} - \omega t)] = \exp[-\mathbf{A} \cdot \mathbf{x}] \exp[i(\mathbf{P} \cdot \mathbf{x} - \omega t)], \quad (5.7)$$

where \mathbf{P} is the propagation vector and \mathbf{A} is the attenuation vector. Both vectors are real valued and in our 1D case, the vectors \mathbf{P} and \mathbf{A} are parallel. $\mathbf{k} = \mathbf{P} + i\mathbf{A}$ is the complex wavevector. In this formulation also the ray parameter and velocity are complex magnitudes.

To calculate the amplitudes the following formula is used (Slawinski and Krebes, 1991)

$$u_z = \int_{-\infty}^{\infty} \frac{Y}{L} S(\omega) \exp[i\omega(\tau - t)] b_z d\omega, \quad (5.8)$$

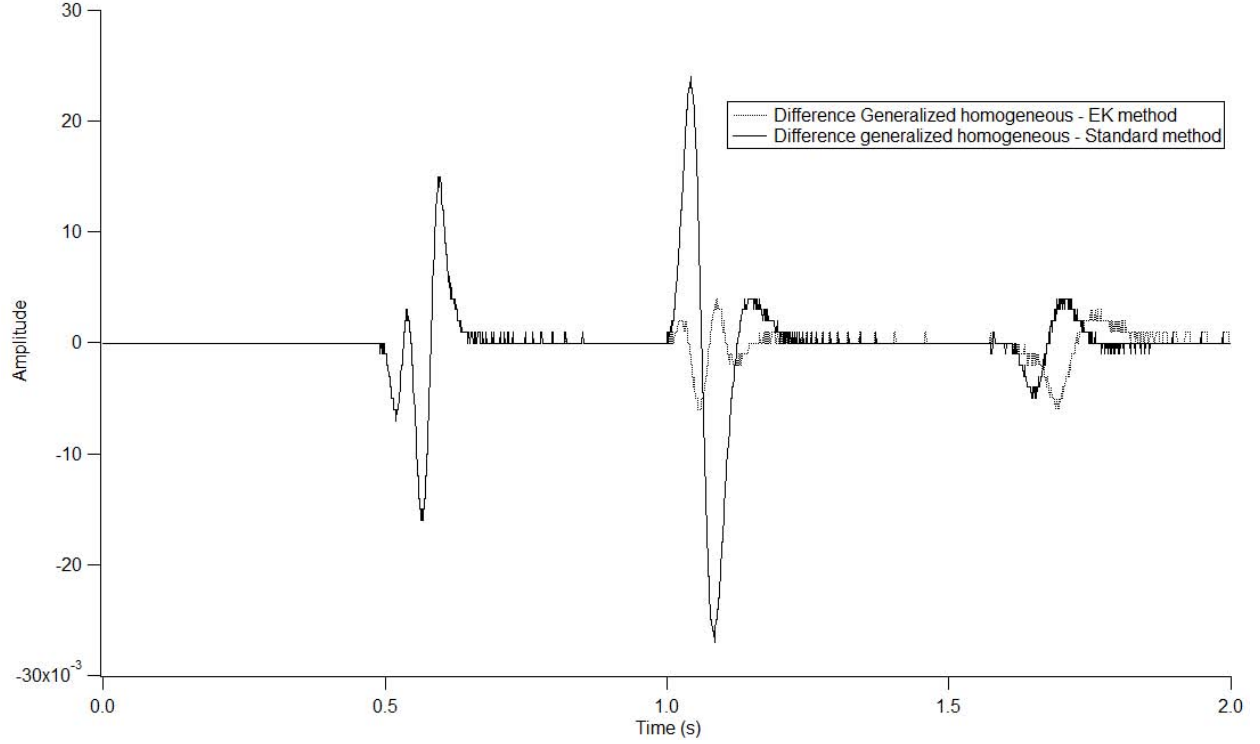


Figure 5.6: Graph of the difference between the generalized finite difference method and the EK and standard method for welded contact.

where Y is the product of the particle displacement reflection and transmission coefficients at the interfaces and L is the geometrical spreading factor (Slawinski and Krebs, 1991). In our case we do not consider any geometrical spreading since our model is one-dimensional and therefore $L = 1$. b_z is the vertical component of a vector that gives the direction of the compressional wave particle motion at the receiver.

In order to include the non-welded contact in the ray tracing algorithm we modified the calculation of the reflection and transmission coefficients in the code developed by Dr. Krebs. The equation for the reflection coefficients in the normal incidence case can be written (Zhu and Snieder, 2002):

$$R = \frac{1 - i\omega Z_2 \eta - Z_2/Z_1}{1 - i\omega Z_2 \eta + Z_2/Z_1}, \quad (5.9)$$

where Z_1, Z_2 are the impedances of media 1 and 2 respectively, η is the compliance and ω is the angular frequency. For $\eta = 0$ the equation is reduced to the equation for the welded

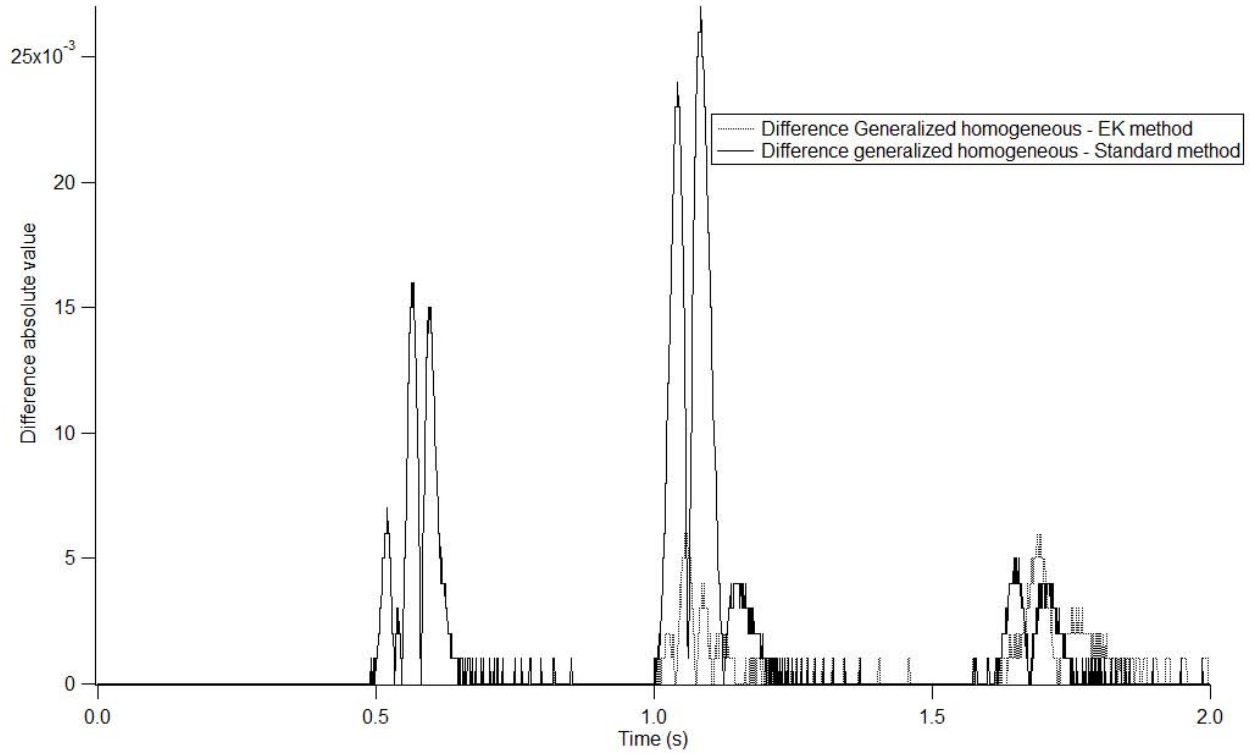


Figure 5.7: Graph of the absolute value of the difference between the generalized finite difference method and the EK and standard method.

contact case.

In Figure 5.8 we can observe the finite difference result (solid line) along with the result provided by the analytical solution (dashed line), for the reflected wave coming from the first interface in welded contact. Although minor differences are present in both seismographs, they agree very closely.

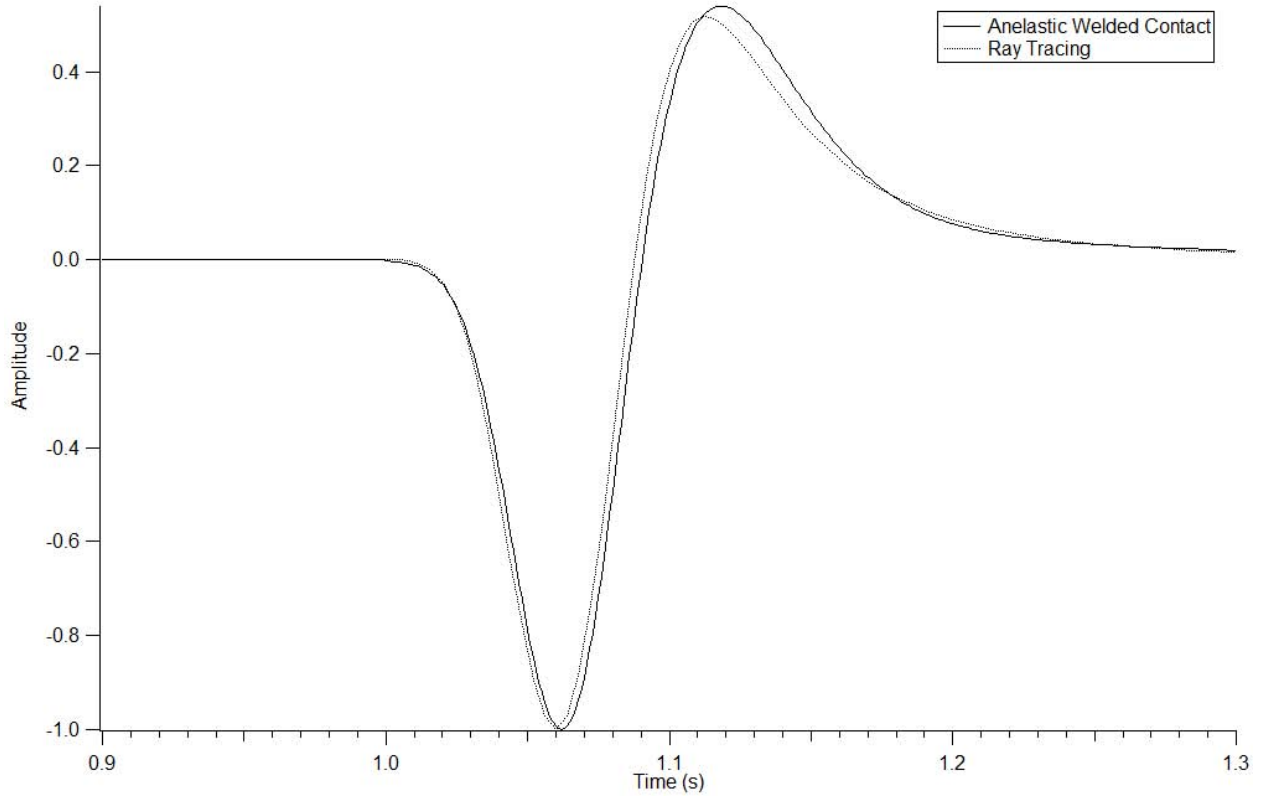


Figure 5.8: Comparison between the FD for the welded contact case (solid line) and the analytical solution (dashed line). Both graphs are normalized to a maximum amplitude of unity.

5.3 EFFECT OF COMPLIANCE ON THE REFLECTED WAVE

In order to study the effect of non-zero compliance values or non-welded contact in the boundary conditions we focused on two cases. A first set of simulations were done by placing the receiver at 500m and observing the reflected wave. For the second set of experiments the geometry of the problem was changed by placing the receiver at 800m. The objective of the different geometries is to measure to what extent the compliance values affect the amplitude of both the reflected and the transmitted waves. The second case will be seen in the next section.

In figure 5.9 we can observe the change in the reflected wave for values of the compliance ranging from 0.001 to 0.09m/GPa. As the value of the compliance decreases, the waveform amplitudes approaches the values of the welded contact case. For very small values of the

compliance the first effect to be observed is a small delay in the travel-time of the wave. As compliance values continues to increase a change of the phase of the wave can be observed. For values of the compliance $\eta_N \geq 0$ the non-welded contact starts to become decoupled. For a sufficient large value of the compliance the returning pulse shows the same polarity as the incident wave. In the limit $\eta_N \rightarrow \infty$ the fracture will be totally decoupled, hence we will be in the presence of the free surface case. In figure 5.10 we can observe how the change in the phase starts for a value of compliance around $\eta_N = 0.004$.

Another factor to take into account is the change in the values of the amplitudes. The amplitudes of the reflected waves, in the case when $\eta_N \neq 0$, are larger than the welded case. This effect can be explained on the basis that for the non-welded case both the impedance contrast and the displacement discontinuity are responsible for the reflection. In the welded contact case the amplitude of the reflected wave is affected only by the impedance contrast.

It is also very interesting to look at the values of the amplitude of the second reflection. As the fracture becomes decoupled, due to the increase of compliance values, a decrease in the amplitude of the energy coming from the second interface is expected, since less energy is transmitted across the first interface. Figure 5.11 shows this effect.

Figure 5.12 show an overlay of the generalized scheme and the ray theory for different values of the compliance. For very small and very large values of the compliance both seismograms are very close. However as can be observed in the graph, for values of the compliance around $0.01m/GPa$ we can find the largest difference in our results. Around this value is when the interface starts to become decoupled. This might point to a difference between both methods in the treatment of the boundary conditions at the interface.

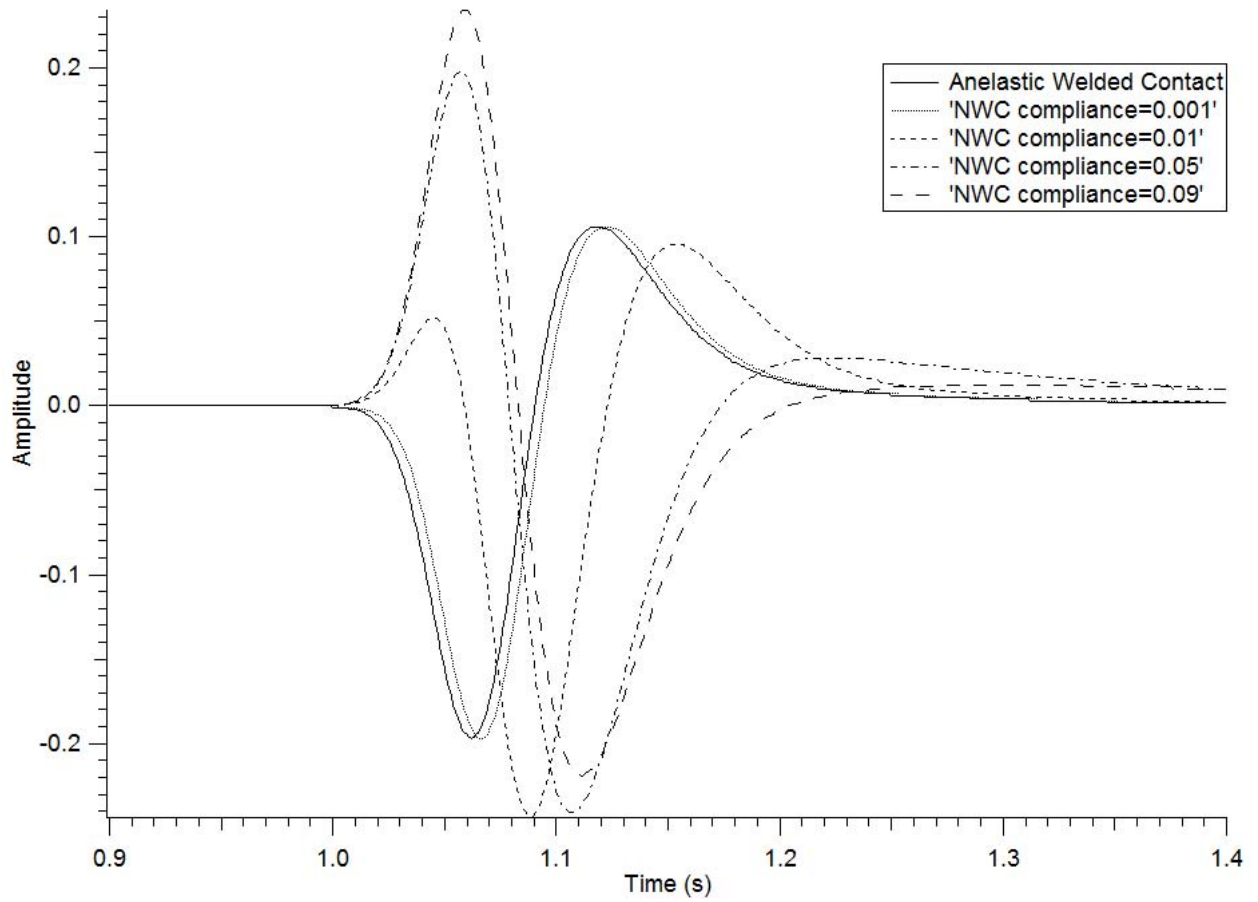


Figure 5.9: Effect of compliance on the reflected wave coming from the first interface.

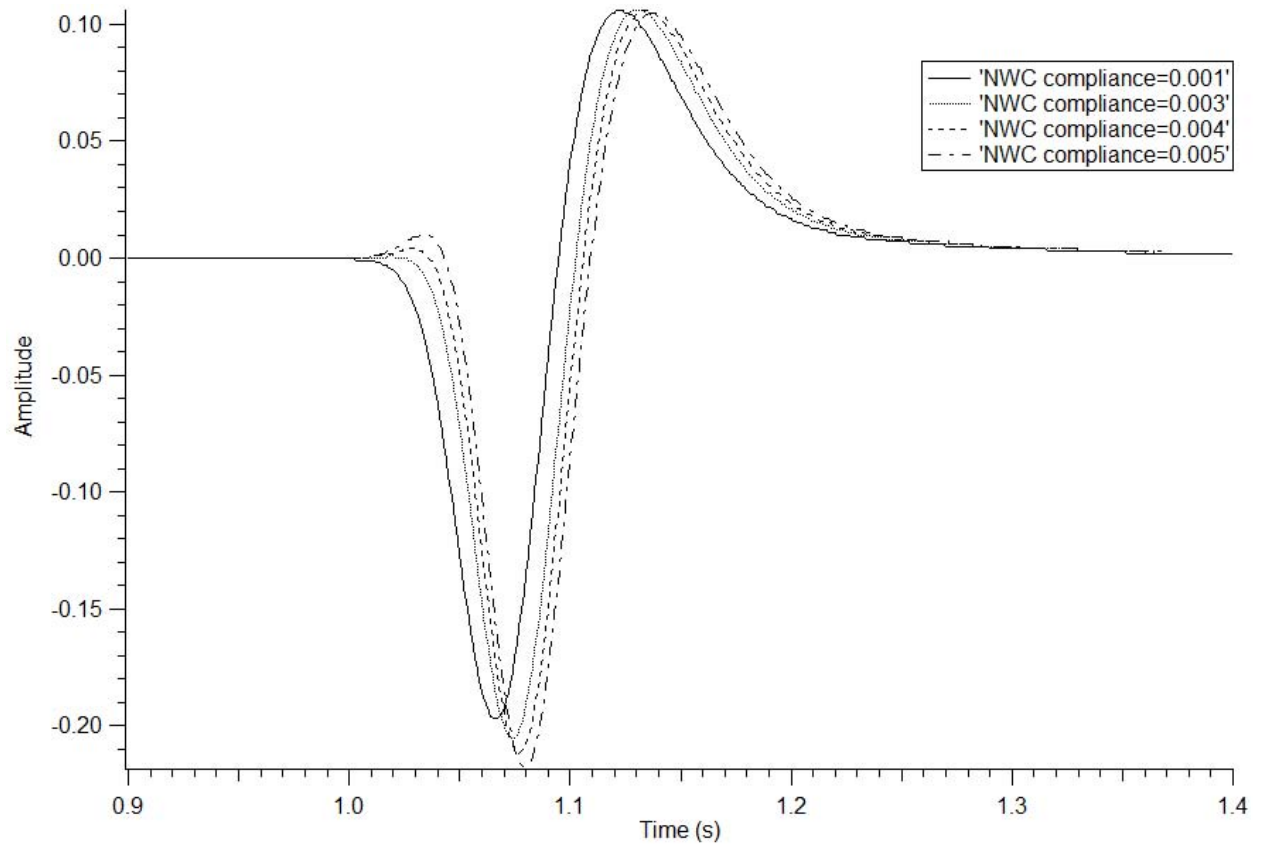


Figure 5.10: Reflection from the first interface for a range from 0.001 to 0.005.

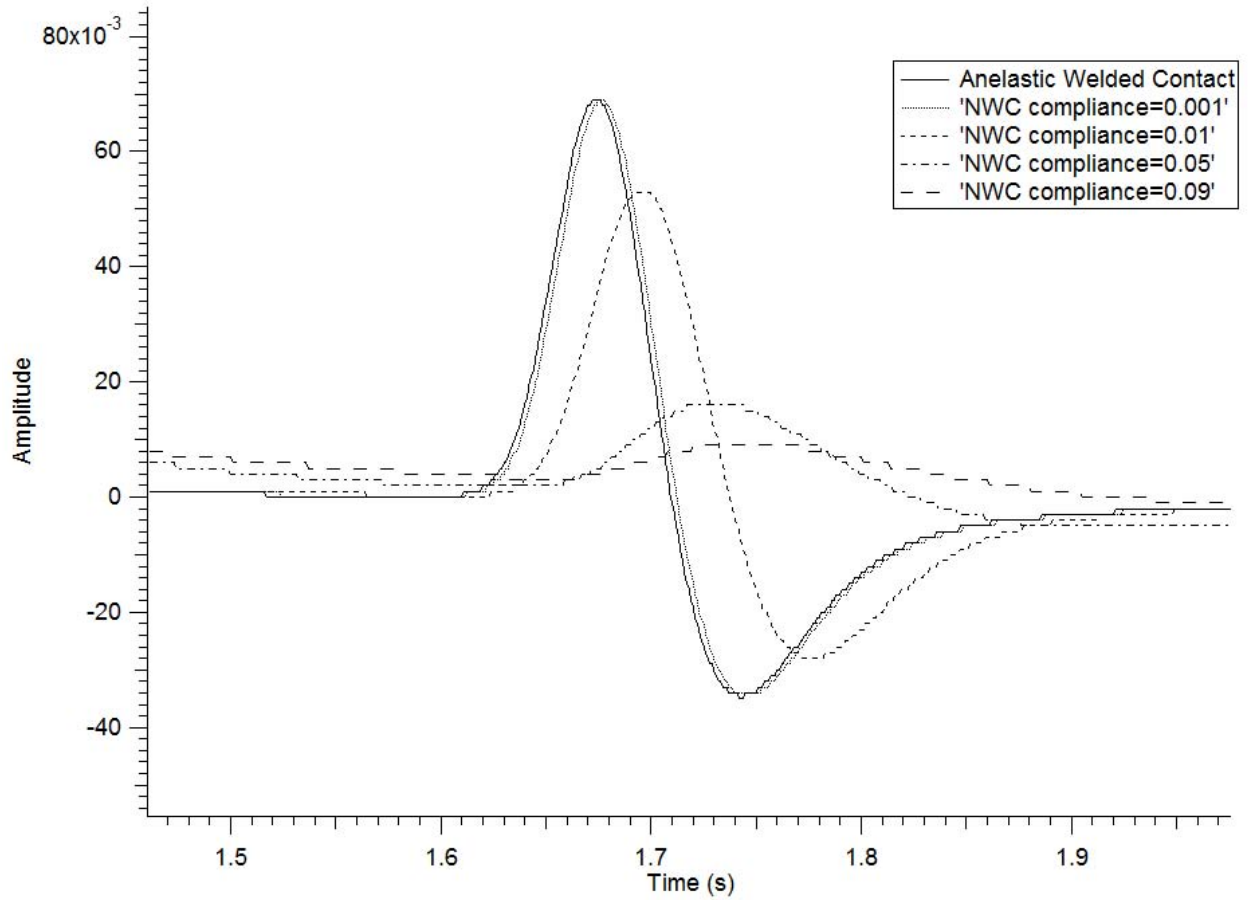


Figure 5.11: Effect of compliance on the reflected wave coming from the second interface. As the first fracture becomes decoupled less energy is transmitted to the second interface.

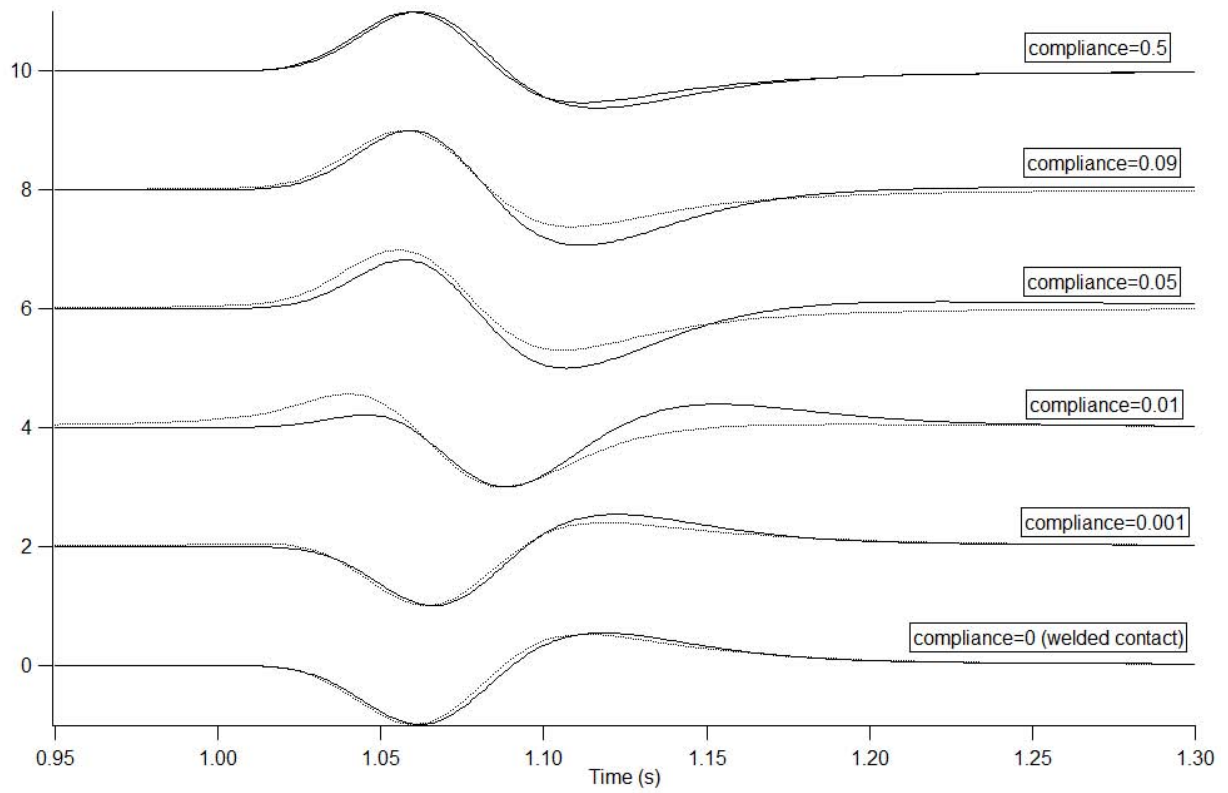


Figure 5.12: Effect of compliance on the reflected wave coming from the first interface (solid line) compared to the analytical solution (dashed line)

5.4 EFFECT OF THE COMPLIANCE ON THE TRANSMITTED WAVE

Next we consider the problem of transmission of energy across the first interface. In figure 5.13 we can observe the specified geometry for this simulation. The only difference with the previous case is that the receiver was placed with an offset of 800 meters from the source, effectively placing it within the second layer. In figure 5.14 we can observe how the increase of compliance values affects absorption after the initial pulse goes through the interface. For small values of the compliance or high values of the stiffness there is a small delay in the travel-time. As the value of the stiffness decreases there is a decrease in the amplitude of the transmitted pulse since more energy is reflected at the interface. In figure 5.15 we can observe how the spectrum of the transmitted pulse changes for different values of compliance. For large values of the compliance a large portion of the amplitudes is reflected resulting in lower spectral amplitudes. The non-welded contact interface acts as a low-pass filter for the transmitted wave. This behavior is in accordance with experimental results where the presence of fractures induce a decrease in the amplitudes of the propagating waveforms, a low-pass filter effect and a delay in the traveltime (Pyrak-Nolte et al., 1990), (Li and Pyrak-Nolte, 2010).

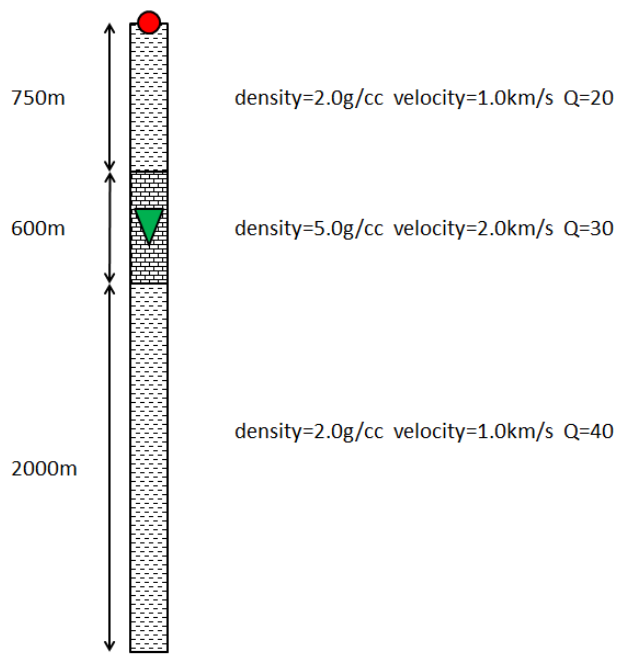


Figure 5.13: Problem geometry and model for the transmitted wave.

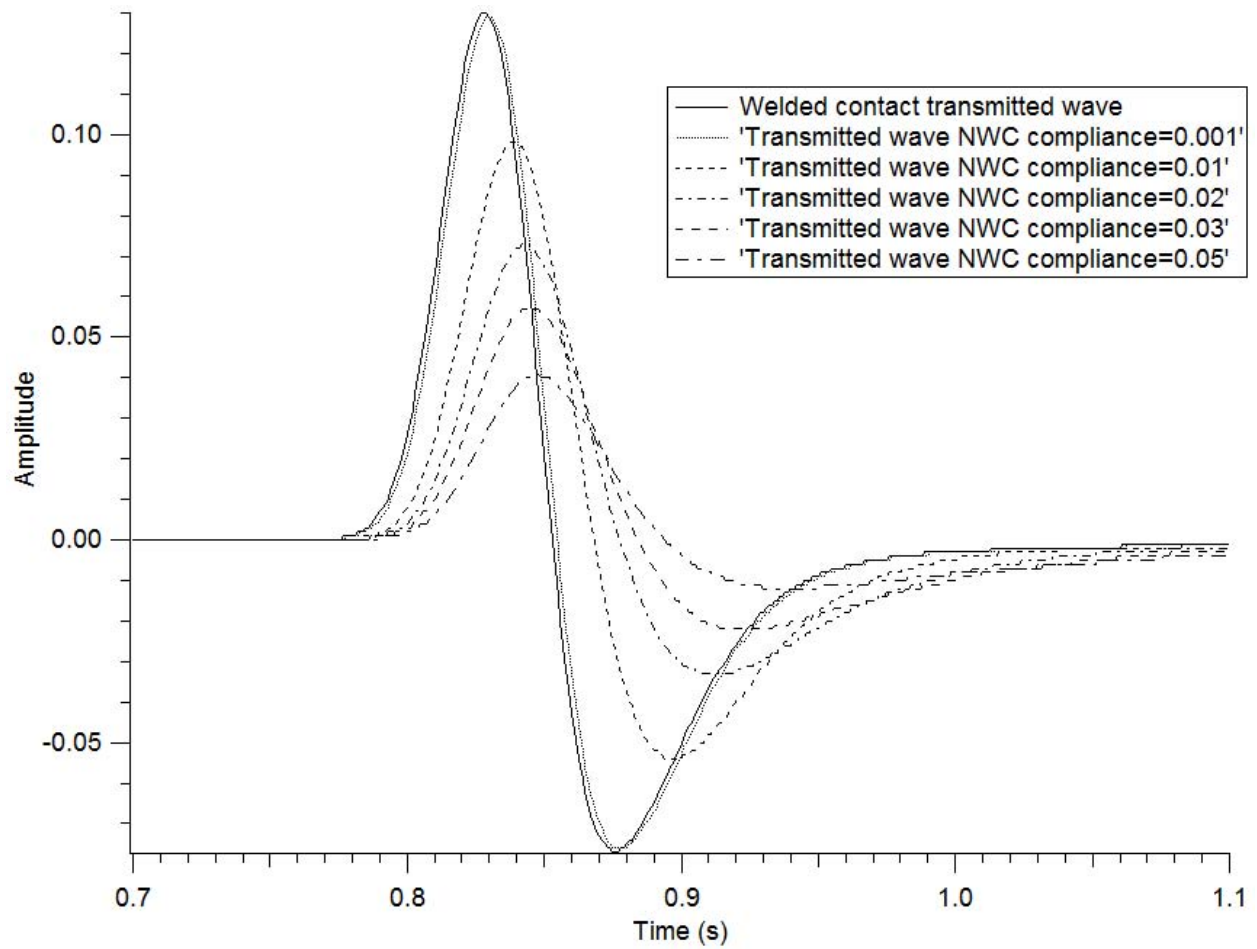


Figure 5.14: Effect of compliance on the transmitted wave.

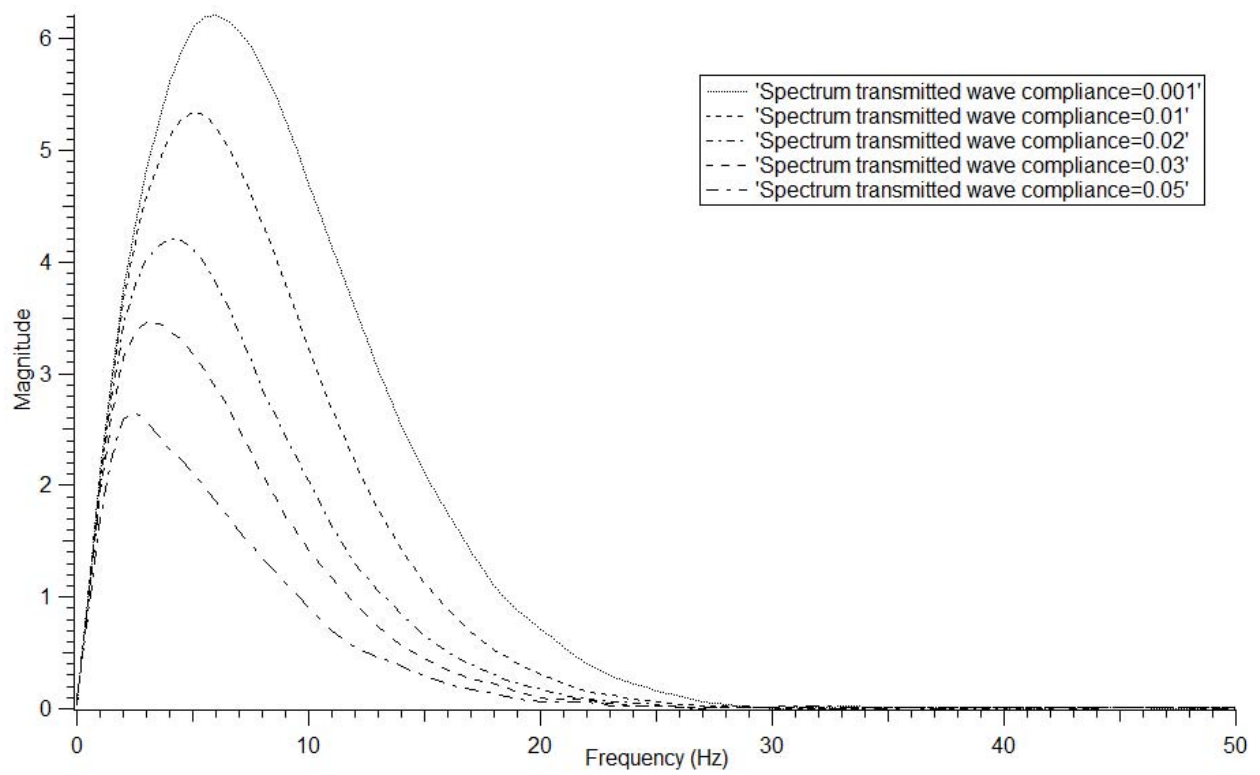


Figure 5.15: Effect of compliance on the power spectrum of the transmitted wave. The increase of the compliance values act as a low-pass filter for the pulse.

5.5 EFFECT OF THE ANELASTICITY IN THE TRANSMITTED WAVE

In order to consider the effect of the anelasticity in the transmitted wave we fix the value of the compliance in the non-welded contact and observe if there are any changes if we take anelasticity into account. Moreover it is very interesting to compare this result with simulations where the elastic case ($Q = \infty$) has been implemented for all the layers and the value of compliance is changed. In figure 5.16 we have plotted the results of a wave transmitted across a welded contact interface between two anelastic media and a non-welded contact interface between two elastic media. The value of compliance has been varied from 0.005 to 0.04m/GPa for the interface located between two lossless media. The increase of the compliance for the non-welded contact produces a response that resembles attenuation in the anelastic case. On the other hand if the values of Q are decreased, amplitudes are strongly attenuated. In other words, the response of the non-welded contact elastic case resembles that of the welded contact between two anelastic media for the transmitted case. There are however some differences. The introduction of very small values of Q produces a larger travel-time delay in the transmitted pulse. The negative section of the pulse is almost completely attenuated as $\eta_N \rightarrow 0.04m/GPa$. In addition the introduction of viscoelasticity in the model causes a larger spreading in the wavelength defocusing the energy of the pulse. However this effect is less noticeable for the case where both media are elastic and the interface is in non-welded contact.

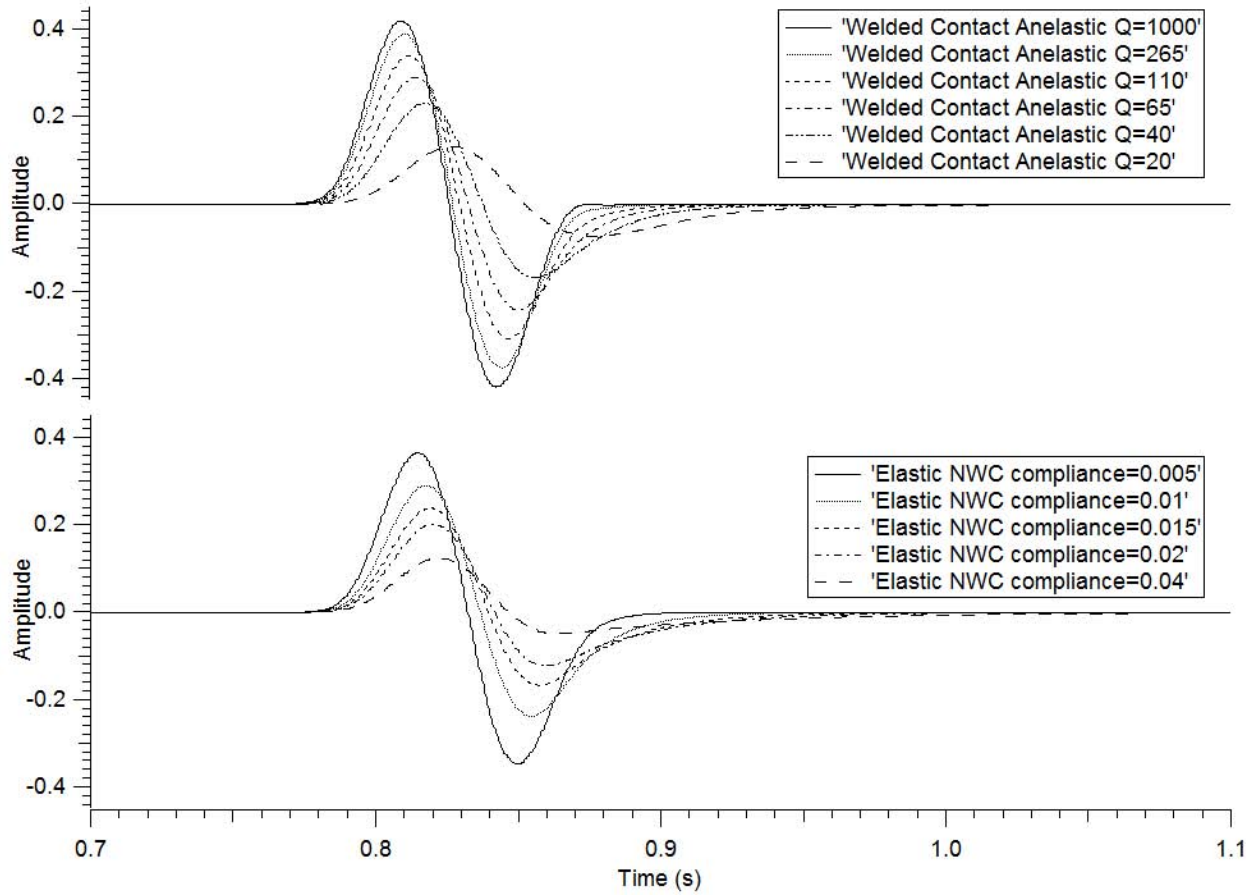


Figure 5.16: Effect of viscoelasticity on the transmitted wave compared to the effect of the non-welded contact between two elastic media. For the anelastic case the value of Q is the same for both layers.

5.6 EFFECT OF THE ANELASTICITY IN THE REFLECTED WAVE

If we repeat the experiment described in the previous section and take a look instead at the reflected wave in figure 5.17 we found larger differences in comparison with the transmitted wave case. When the compliance is increased the phase of the wave in the elastic case with non-welded contact changes as well. The value of the phaseshift for a large value of the compliance ($\eta_N > 0.04$) is 180° . In other words when the fracture is totally decoupled the reflected pulse has opposite polarity compared with the reflected wave coming from a welded contact interface.

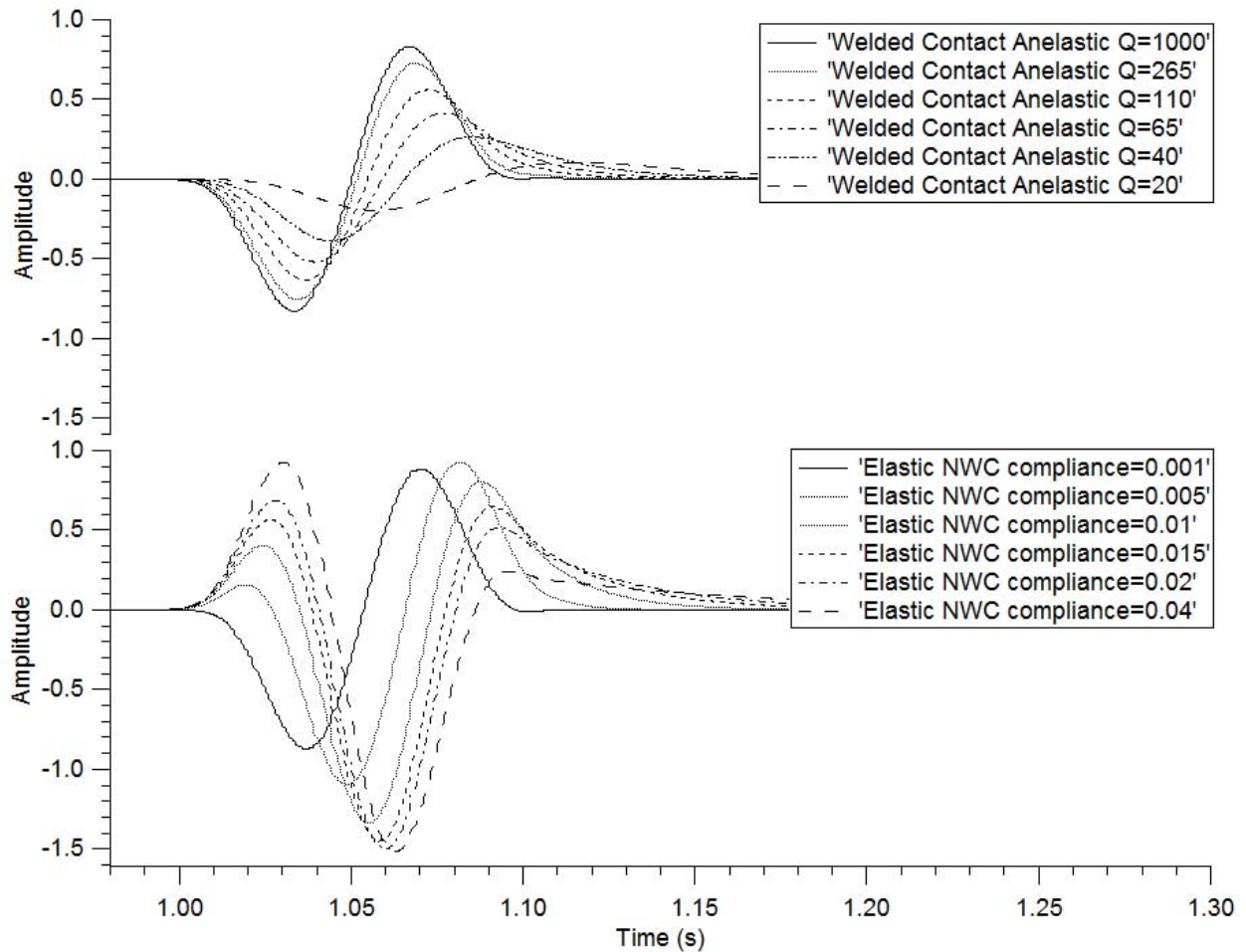


Figure 5.17: Effect of viscoelasticity on the reflected wave compared to the effect of the non-welded contact between two elastic media.

For values of the compliance $\eta_N \leq 0.001m/GPa$ the shapes of both pulses are identical

since we are taking into consideration the same physical experiment where the boundary can be considered in welded contact between two elastic media.

If we consider the case where the incident medium is elastic and the transmission medium is anelastic we can observe the effect of the non-welded contact on the reflected wave. In the following example we chose a value of $\eta_N = 0.0015$ for the non-welded contact because around this value the fracture starts to become decoupled. In figure 5.18 can be seen the elastic-anelastic case with a non-welded contact interface compared to the elastic-anelastic case with a welded contact interface. For an increase in the values of Q from 20 to 1000 in the transmission viscoelastic medium there is no significant difference whether the boundary is in welded contact or not.

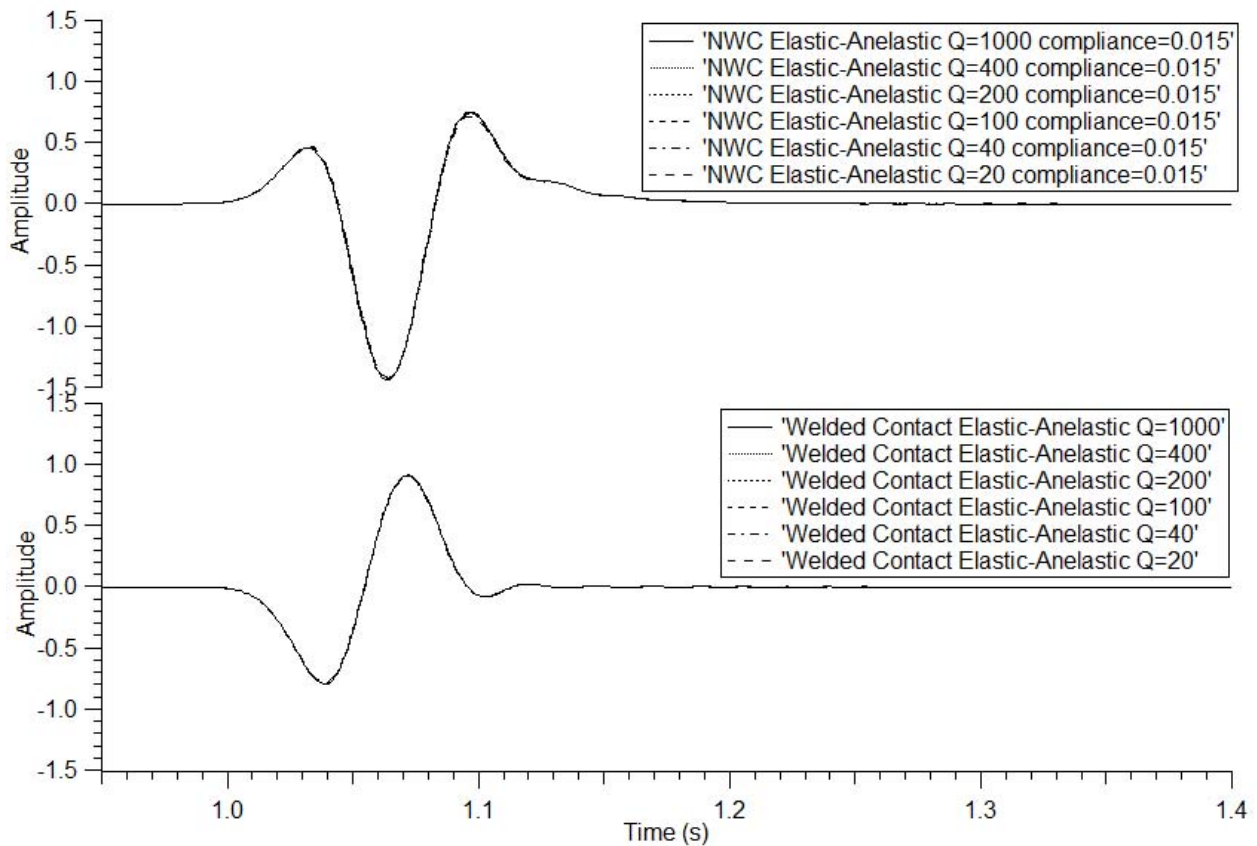


Figure 5.18: The graph shows the reflected wave produced by an interface located between an elastic incident medium and an anelastic transmitted medium. In the upper section the interface between the two media is in non-welded contact for values of the compliance around $0.015m/GPa$. The lower section shows the seismic response when the interface between the two media is in welded contact.

5.7 NON-WELDED CONTACT LAYERED MEDIUM

One of the most interesting questions that arose during the preparation of this work was to know how the waveform of a wave would be affected, assuming every interface of a medium in non-welded contact. In other words what is the effect on the amplitude of the waves of a finely layered fractured medium. In order to answer this question we build the model that can be seen in figure 5.19 and compare the response of this medium to the response of a wave propagating in an anelastic medium. The upper section of the figure shows an elastic medium where every boundary is in non-welded contact. The results obtained with this model are compared with the results of an anelastic medium where every boundary is in welded contact. The velocity and the density of the medium are 1000m/s and 2g/cc respectively for both cases. The offset between source and receiver is 500m. For the elastic medium case there are 200 interfaces in non-welded contact between the source and the receiver.

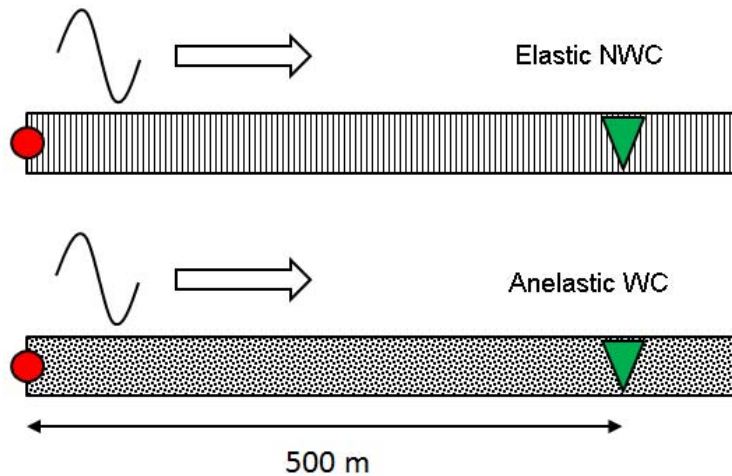


Figure 5.19: The upper section shows an elastic model where every boundary is in non-welded contact and the background medium is elastic. The lower section shows an anelastic medium with every interface in welded contact.

In figure 5.20 we can observe the result of the aforementioned simulations. We selected a range of compliance values from 0 to $0.00003m/GPa$ and for the anelastic case a value of Q ranging from 1000 to 40. In the upper section it is shown that a very small variation of

the compliance causes a very large amount of travel-time delay in the medium while minor changes of the amplitudes can be observed. A change in the order of $0.0001m/GPa$ in the compliance for all the boundaries in the model can cause a $2ms$ travel-time delay. In figure 5.21 we can observe that the dependence between travel-time delay and the compliance follows a linear relationship. For the case where the medium is anelastic the introduction of increasingly smaller values of Q does not produce a significant change in the travel-time. Note that dispersion effects were not included in this work. Therefore the viscoelastic properties of the material cannot be modeled on the base of a heavily fractured model with particle displacement discontinuity if the background medium is lossless. To correctly model this behavior it is necessary to include in the linear slip boundary conditions a velocity discontinuity in addition to the particle displacement (Carcione et al., 2012).

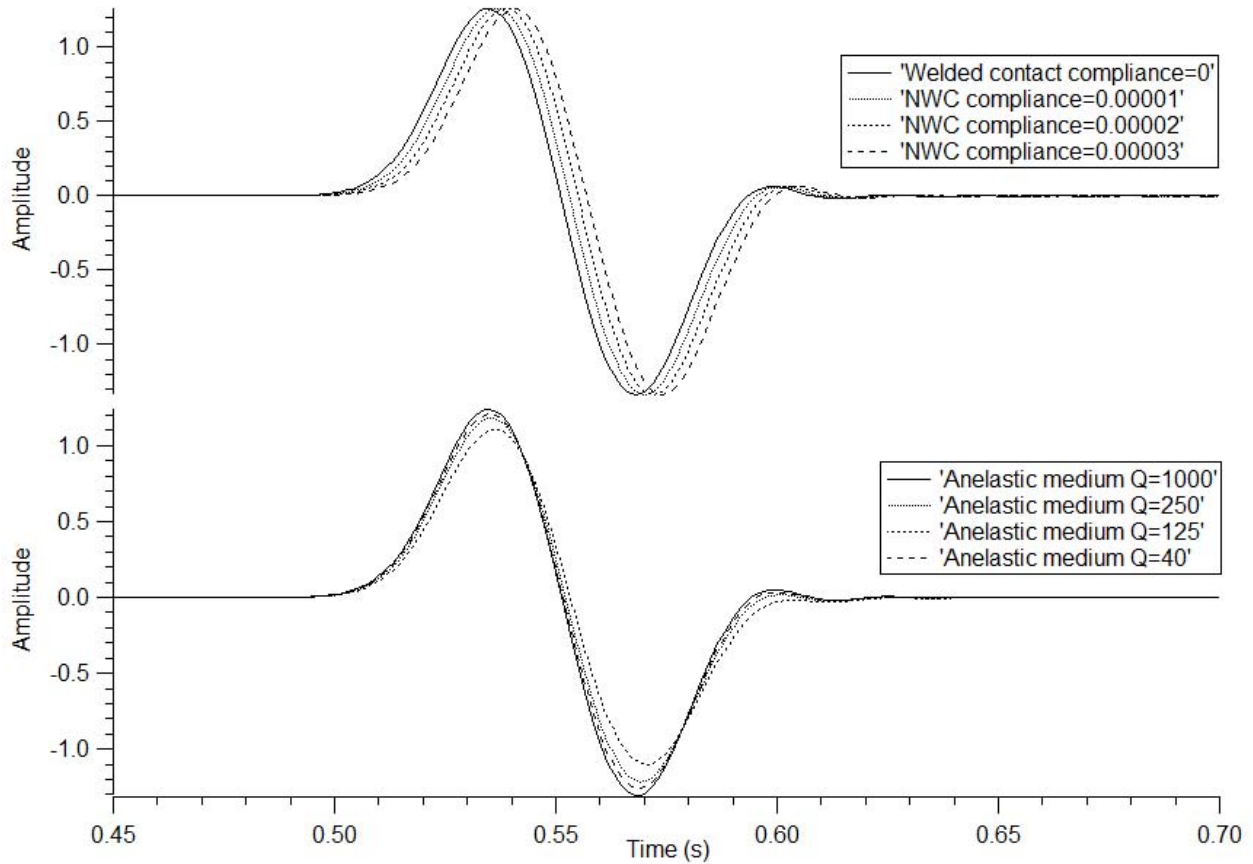


Figure 5.20: The upper section show the different waveforms of the direct wave for different values of the compliance assuming every boundary of the grid in non-welded contact in the elastic medium. The lower section show the different waveforms of the direct wave for different values of Q in an anelastic medium.

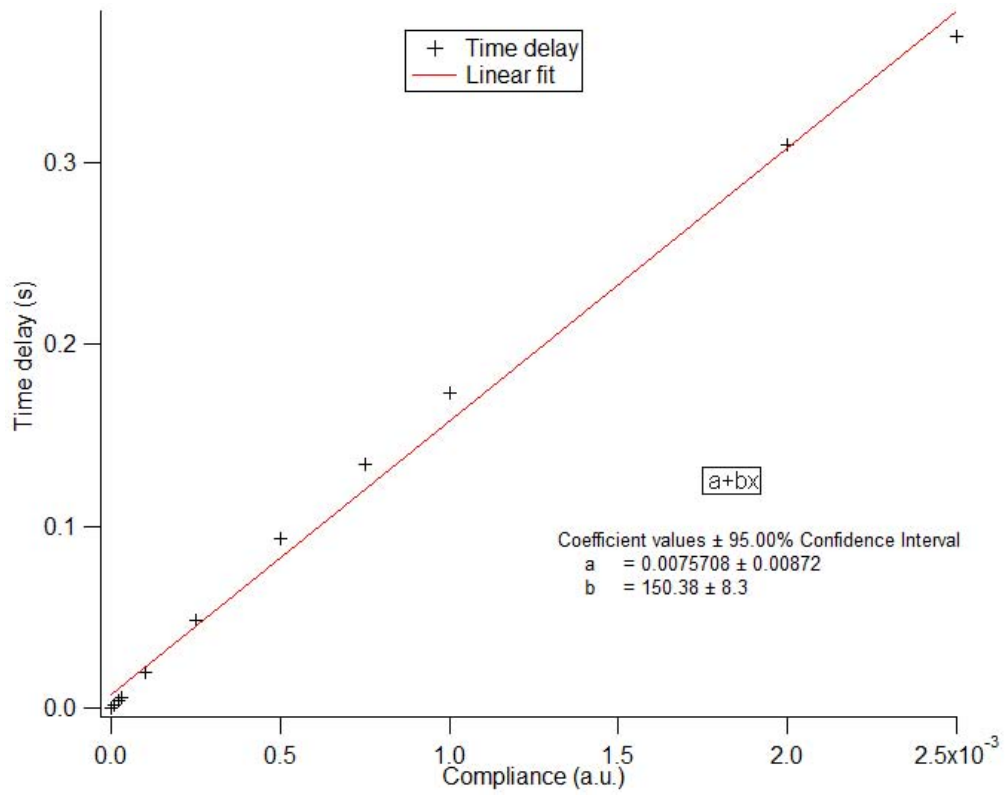


Figure 5.21: Travel-time delay vs compliance showing a linear dependence between the two factors.

Chapter 6

CONCLUSIONS

The finite difference formulation of the non-welded contact developed in this work using the linear slip boundary condition is an effective method to simulate real fractures. The numerical modeling using the fictitious point scheme proposed by Korn and Stöckl is straightforward and allows for the inclusion of the non-welded contact formulation into a finite difference scheme. Thus a generalized homogeneous scheme is obtained that effectively include non-welded contact boundary conditions.

I have reviewed different approaches to the problem of the inclusion of viscoelastic properties in numerical wave modeling. The generalized Maxwell rheology allows one to introduce a complex frequency dependent viscoelastic modulus $M(\omega)$ that transforms the differential equation of motion into an algebraic equation. This is accomplished by finding a constitutive relation based on a discrete spectrum of multiple relaxation mechanisms. The solution found effectively solves the problem of the convolutional form of Boltzmanns superposition principle in the time domain. In addition the coefficients of the series approximation are not merely analytical values but represent the physical properties of the J elements composing the viscoelastic model.

I also have analyzed two finite difference formulations of the viscoelastic problem and compared their relative advantages. The Emmerich and Korn and the standard scheme yield identical results when reduced to the homogeneous case and minor differences for the heterogeneous case even when the treatment of interfaces is different in both cases. In addition memory requirements for the standard method are considerable larger than for the EK. Nevertheless given the actual advances in processing power this limitation is irrelevant for the analysis of the 1D case. Another advantage of the finite difference implementation

proposed by Krebes and Quiroga-Goode is that analysis of the theoretical background is easier and does not require averaging medium properties around the boundary.

In this work I have also proposed a finite difference scheme for solving the non-welded contact problem in anelastic media. By using the scheme proposed by Emmerich and Korn, consisting in the extrapolation of the media across the boundary, I solve the linear slip problem for the non-welded contact taking into consideration memory variables. This problem lead to a system of equations for the boundary conditions. The solution to this system of equations describes the conservation of stress across the boundary and the discontinuity in the displacement values. For this purpose I used a relaxation function that describes the anelastic properties of the material according to the Maxwell-Wiechert rheology and introduced memory variables for the description of the stress-strain relationship.

The numerical results obtained in a very simple one-dimensional model showed that the presence of an interface in non-welded contact acts as a low-pass filter and also produces a travel-time delay in the transmitted signal. I have reviewed how the heterogeneous finite difference scheme produces very similar results to previous viscoelastic formulations for the welded contact case. The method developed has also been compared with an analytical solution for the proposed model. The results of these comparisons validates the finite difference scheme obtained. In addition I have measured the combined effect of both the non-welded contact and viscoelasticity on the model as well as the effect of each one of them individually. The developed heterogeneous finite difference scheme effectively combine both phenomena into a unified formulation.

Bibliography

- J. D. De Basabe and M. K. Sen. Grid dispersion and stability criteria of some common finite-element methods for acoustic and elastic wave equations. *Geophysics*, 72(6):81–95, NOVEMBER-DECEMBER 2007.
- J. Behura, Batzle M., J. Hofmann, and J. Dorgan. Heavy oils: their shear story. *Geophysics*, 72:175–183, 2007.
- J. M. Carcione. Elastodynamics of a non-ideal interface: Application to crack and fracture scattering. *Journal of Geophysical Research*, 101(B12):28177–28188, 1996.
- J. M. Carcione, D. Kosloff, and R. Kosloff. Wave propagation simulation in a linear viscoelastic medium. *Geophysical Journal*, 95:597–611, 1988.
- J. M. Carcione, G. Herman, and A. P. E. ten Kroode. Seismic modeling. *GEOPHYSICS*, 67(4):1304–1325, 2002.
- J. M. Carcione, S. Picotti, and J. E. Santos. Numerical experiments of fracture-induced velocity and attenuation anisotropy. *Geophysical Journal International*, 191:1179–1191, 2012.
- R. M. Christensen. *Theory of Viscoelasticity: An Introduction*. Academic Press, 1971.
- Richard T. Coates and Michael Schoenberg. Finite-difference modeling of faults and fractures. *Geophysics*, 60(5):1514–1526, 1995.
- S. M. Day and J. Bernard Minster. Numerical simulation of attenuated wavefields using a pade approximant method. *Geophys. J. R. astr. SOC*, 78:105–118, 1984.
- H. Emmerich and M. Korn. Incorporation of attenuation into time-domain computations of seismic wave fields. *Geophysics*, 52(9):1252–1264, 1987.

- B. Gu, K. T. Nihei, , and L. R. Myer. Numerical investigation of fracture interface waves. *Journal of the Acoustical Society of America*, 102(1):120–127, 1997.
- M. Korn and H. Stöckl. Reflection and transmission of love channel waves at coal seam discontinuities computed with a finite difference methods. *Journal of Geophysics*, 50: 171–176, 1982.
- E. Krebs and G. Quiroga-Goode. A standard finite-difference scheme for the time-domain computation of anelastic wavefields. *Geophysics*, 59(2):290–296, 1994.
- E. S. Krebs. Theoretical seismology. *Lecture notes*, 2010.
- W. Li and L. J. Pyrak-Nolte. Seismic wave propagation in fractured carbonate rock. *Proceedings of the Project Review, Geo-Mathematical Imaging Group*, 1:211–220, 2010.
- H. Liu, D. L. Anderson, and H. Kanamori. Velocity dispersion due to anelasticity; implications for seismology and mantle composition. *Geophys. J. R. astr. Soc.*, 47:41–58, 1976.
- B. G. Mikhailenko. Numerical experiment in seismic investigations. *Geophys. J.*, 58:101–124, 1985.
- Peter Moczo. Finite-difference technique for sh-waves in 2-d media using irregular grids - application to the seismic response problem. *Geophysical Journal International*, 99:321–329, 1989.
- A. S. Nowick and B. S. Berry. *Anelastic relaxation in crystalline solids*. Academic Press, 1972.
- L. J. Pyrak-Nolte. Seismic visibility of fractures. *PhD thesis, University of California*, 1988.

- L. J. Pyrak-Nolte. The seismic response of fractures and the interrelations among fracture properties. *International Journal of Rock Mechanics, Minearology Sciences and Geomechanics*, 33(8):787–802, 1996.
- L. J. Pyrak-Nolte, L. R. Myer, and Neville G. W. Cook. Transmission of seismic waves across single natural fractures. *Journal of Geophysical Research*, 95(B6):8617–8638, 1990.
- M. Schoenberg and J Douma. Elastic wave propagation in media with parallel fractures and aligned cracks. *Geophysical Prospecting*, 36:571–590, 1988.
- Michael Schoenberg. Elastic wave behaviour across linear slip interfaces. *Journal of the Acoustical Society of America*, 68(5):1516–1521, 1980.
- M. Slawinski and E. S. Krebes. On raytracing in an elastic-anelastic medium. *Bulletin of the Seismological Society of America*, 81(2):667–686, April 1991.
- R. Slawinski. Finite-difference modeling of seismic wave propagation in fractured media. *PhD Thesis*, 0-612-49538-8, 1999.
- R. Slawinski and E. S. Krebes. Finite-difference modeling of sh-wave propagation in non-welded contact media. *Geophysics*, 67(5):1656–1663, September-October 2002.
- H. Tal-Ezer, J. M. Carcione, and D. Kosloff. An accurate and efficient scheme for wave propagation in linear viscoelastic media. *Geophysics*, 55:1366–1379, 1990.
- Y. Zhu and R. Snieder. *Reflected and transmitted waves from fault zones*. SEG International Exposition and 72nd Annual Meeting, 2002.